



HAL
open science

Nanosized tubular clay minerals as inorganic nanoreactors for energy and environmental applications: A review to fill current knowledge gaps

Yassine Naciri, Mohamed Nawfal Ghazzal, Erwan Paineau

► To cite this version:

Yassine Naciri, Mohamed Nawfal Ghazzal, Erwan Paineau. Nanosized tubular clay minerals as inorganic nanoreactors for energy and environmental applications: A review to fill current knowledge gaps. *Advances in Colloid and Interface Science*, 2024, 326, pp.103139. 10.1016/j.cis.2024.103139 . hal-04525942

HAL Id: hal-04525942

<https://hal.science/hal-04525942v1>

Submitted on 29 Mar 2024

HAL is a multi-disciplinary open access archive for the deposit and dissemination of scientific research documents, whether they are published or not. The documents may come from teaching and research institutions in France or abroad, or from public or private research centers.

L'archive ouverte pluridisciplinaire **HAL**, est destinée au dépôt et à la diffusion de documents scientifiques de niveau recherche, publiés ou non, émanant des établissements d'enseignement et de recherche français ou étrangers, des laboratoires publics ou privés.

Nanosized tubular clay minerals as inorganic nanoreactors for energy and environmental applications: A review to fill current knowledge gaps

Yassine Naciri^{1,2}, Mohamed Nawfal Ghazzal^{2,*} and Erwan Paineau^{1,*}

¹Université Paris-Saclay, CNRS, Laboratoire de Physique des Solides, 91405 Orsay, France

²Université Paris-Saclay, CNRS, UMR8000, Institut de Chimie Physique, 91405, Orsay, France.

* mohamed-nawfal.ghazzal@universite-saclay.fr; erwan-nicolas.paineau@universite-paris-saclay.fr

Abstract

Modern society pays further and further attention to environmental protection and the promotion of sustainable energy solutions. Heterogeneous photocatalysis is widely recognized as one of the most economically viable and ecologically sound technologies to combat environmental pollution and the global energy crisis. One challenge is finding a suitable photocatalytic material for an efficient process. Inorganic nanotubes have garnered attention as potential candidates due to their optoelectronic properties, which differ from their bulk equivalents. Among them, clay nanotubes (halloysite, imogolite, and chrysotile) are attracting renewed interest for photocatalysis applications thanks to their low production costs, their unique physical and chemical properties, and the possibility to functionalize or dope their structure to enhance charge-carriers separation into their structure. In this review, we provide new insights into the potential of these inorganic nanotubes in photocatalysis. We first discuss the structural and morphological features of clay nanotubes. Applications of photocatalysts based on clay nanotubes across a range of photocatalytic reactions, including the decomposition of organic pollutants, elimination of NO_x, production of hydrogen, and disinfection of bacteria, are discussed. Finally, we highlight the obstacles and outline potential avenues for advancing the current photocatalytic system based on clay nanotubes. Our aim is that this review can offer researchers new opportunities to advance further research in the field of clay nanotubes-based photocatalysis with other vital applications in the future.

Keywords: Photocatalyst; clay nanotubes; imogolite; halloysite; chrysotile.

32

33 **Introduction**

34 The hasty growth of the global economy and industrialization over the past
35 century has also led to severe problems worldwide. The world's reserve of natural
36 energy is expected to be depleted within the next 50 years [1]. Experts consider
37 global warming and climate change to be a direct consequence of the exponential
38 increase in the consumption of fossil fuels. The increase in industrial pollutants is
39 another consequence of the extensive use of these resources [2–4]. Requirement for
40 developing environmentally friendly and energy-conserving solutions to address
41 environmental remediation.

42 Solar energy represents a highly promising resource due to its unique
43 advantages. It offers an abundant and inexhaustible source of power, surpassing
44 global energy consumption by several times [5–7]. Furthermore, solar energy is
45 environmentally friendly, emitting minimal greenhouse gases, thereby helping to
46 mitigate climate change. According to United Nations Development Programme
47 data, the annual solar energy potential ranges from 1575 to 49387 exajoules (EJ) [8],
48 which greatly exceeds our global annual energy consumption of 559.8 EJ. This
49 remarkable surplus makes solar energy a viable and sustainable solution for driving
50 human development. Numerous fields use solar energy, such as photovoltaics,
51 thermal energy, artificial photosynthesis, solar architecture, and photocatalysis [9–
52 13]. Among them, photocatalysis emerges as a cutting-edge method for harnessing
53 sunlight and expediting molecular conversions to generate solar-derived fuels,
54 primarily hydrogen (H₂), paving the way to a clean and renewable energy source
55 [14,15].

56 In photocatalysis applications, the extensively used photocatalysts such as
57 TiO₂ and ZnO face two primary challenges [16–19]. They have a limited spectral
58 response interval, only capturing a minor portion of the solar spectrum (less than
59 5%), confined to the UV region [4,20]. Additionally, their high charge carrier
60 recombination leads to poor quantum yield [21–25]. As a result, researchers are
61 exploring alternative materials to overcome these limitations. Recent focus has been
62 on 1D nanostructures, whose unique properties hold promise for enhancing
63 photocatalytic activity and expanding its applications.

64 Since the emergence of carbon (C) nanotubes (NTs) at the beginning of the
65 '90s [26], a considerable part of the literature has focused on applying one-
66 dimensional (1D) tubular nanomaterials in numerous fields, including photocatalysis
67 [27–29]. Carbon nanotubes and their inorganic (oxides, sulfides...) analogs have
68 distinctive electronic characteristics such as exceptional electron mobility, the
69 quantum confinement effect, and an extraordinarily large specific surface area [30–
70 32]. The reverse movement of holes and electrons can be promoted by the existence
71 of polarization within the photocatalytic material [33–35]. Numerous studies have
72 reported that the tubular structure led to improved properties. Among them, titania
73 nanotubes exhibited enhanced photocatalytic activity compared to other titania
74 structures [36,37]. Thus, targeting photocatalysts with tubular structures should
75 result in enhanced photocatalytic performance.

76 Although carbon is probably the most studied nanotube material [38–40],
77 various nanotube materials, such as natural clays, have garnered significant interest
78 because of their intriguing characteristics and attributes [41–44]. When referring to
79 clay minerals (or phyllosilicate), we mostly talk about low-dimensional 2D
80 nanostructures. However, clay minerals can adopt also 1D tubular structures. The

81 importance of tubular clay materials as a substituent for expensive CNTs and other
82 nanomaterials is universally recognized [45,46]. Hydrosilicates are considered the
83 most promising nanotube clays minerals due to their ability to scroll spontaneously:
84 chrysotile ($\text{Mg}_3\text{Si}_2\text{O}_5(\text{OH})_4$) [47], halloysite ($\text{Al}_2\text{Si}_2\text{O}_5(\text{OH})_4$) [48–50] and imogolite
85 ($\text{Al}_2\text{SiO}_3(\text{OH})_4$) [51–54]. The crystal structures of imogolite and halloysite combine an
86 aluminum-oxygen dioctahedral sheet covalently bonded to a silicon-oxygen
87 tetrahedra layer for halloysite or to isolated silicon-oxygen tetrahedral in the case of
88 imogolite. For chrysotile, the sheet is classified as trioctahedral as it is mainly
89 composed of magnesium [55]. The differences in the size of sheets and structure led
90 to a bending momentum, transforming the layers into single-walled or multi-walled
91 tubular [56–58]. Additionally, it's worth noting that the unique bending energy of
92 these nanotubes is a key factor in their remarkable stability and mechanical
93 properties, with a Young modulus around approximately 150 GPa for chrysotile [59],
94 140 GPa for halloysite [60], and between 200-600 GPa for imogolite [61]. Recent
95 research on imogolite nanotubes and hydroxyl vacancies in aluminosilicate and
96 aluminogermanate nanotubes has further highlighted the significance of bending
97 energy in influencing their overall mechanical behavior [57,58]. Understanding the
98 bending energy of these nanotubes opens up exciting possibilities for tailored
99 applications in various scientific and engineering fields.

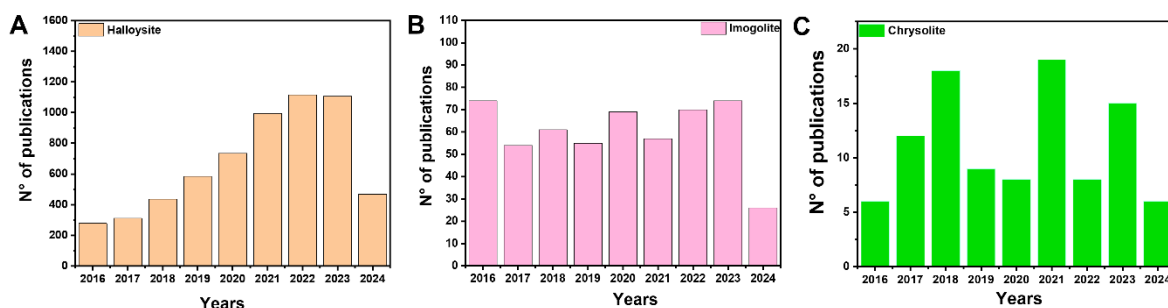
100 Due to their unique properties (e.g., improved light scattering and harvesting,
101 shorter distances for charge transfer, and direct charge separation), materials with a
102 tubular structure have recently found potential in the photocatalysis field [62].
103 Consequently, tubular clay minerals such as imogolite, chrysotile, and halloysite hold
104 the potential to be used, in principle, for such applications. The energy gaps of these
105 nanotubes vary between 4.2 eV to 5.2 eV [63,64], which refers to the minimum

106 energy to excite and separate an electron (e^-) and a hole (h^+) toward the conduction
107 and valence bands, respectively. Additionally, the 1D structure facilitated the
108 effective diffusion of photogenerated electrons and holes [65]. For imogolite
109 nanotubes, recent theoretical investigations have revealed that the curvature of the
110 nanotube wall generates an electronic density distribution and increases the internal
111 electric field, which causes a static force and facilitates the separation of electron-
112 hole pairs [65,66]. Thus, the synergy between polarization and the one-dimensional
113 structure of these photocatalysts is beneficial, as it can enhance the spatial
114 separation of the charge carriers.

115 These clay materials (imogolite, chrysotile, and halloysite) can also be applied
116 as support materials or in conjunction with other photocatalysts to improve the
117 performance of the hybrid structures in degrading numerous pollutants [47,67,68].
118 The improved photocatalytic efficiency results from the synergistic interaction of the
119 unique characteristics of these clay materials, such as their exceptional light
120 absorption, large specific surface area, and visible light absorption ability. It was
121 noted that the halloysite was used in broader applications than the chrysotile and
122 imogolite. This is due to the advantageous attributes of halloysite, such as its
123 affordability and low toxicity, which surpass those of chrysotile [69]. While imogolite
124 is not produced in large quantities yet their efficiency is greater than halloysite. The
125 increasing fascination with halloysite is evident in the rising count of scientific
126 publications and patents over the past decade (**Fig.1**).

127 As far as we know, this review is the first attempt to thoroughly examine
128 recent advances in synthesizing and applying nanosized tubular clay, specifically
129 halloysites, chrysotile and imogolites, as true photocatalysts, or in combination with
130 other semiconductors for heterogeneous photocatalysis, with a particular focus on

131 their properties for energy and environmental applications. After a brief preamble on
 132 the principles of photocatalysis, we focus on analyzing the synthesis, structural,
 133 physiochemical properties, and photocatalytic activity of clay nanotubes (imogolite
 134 nanotubes (INTs), halloysite nanotubes (HNTs) and chrysolite (CINTs)). We
 135 introduce the significance of using nanotube architectures in photocatalysis and
 136 discuss the polarization effect's role. This review subsequently addresses the
 137 processes that improve photocatalyst performance when combined with tubular clay.
 138 Lastly, research opportunities for tubular clay photocatalyst material are proposed.



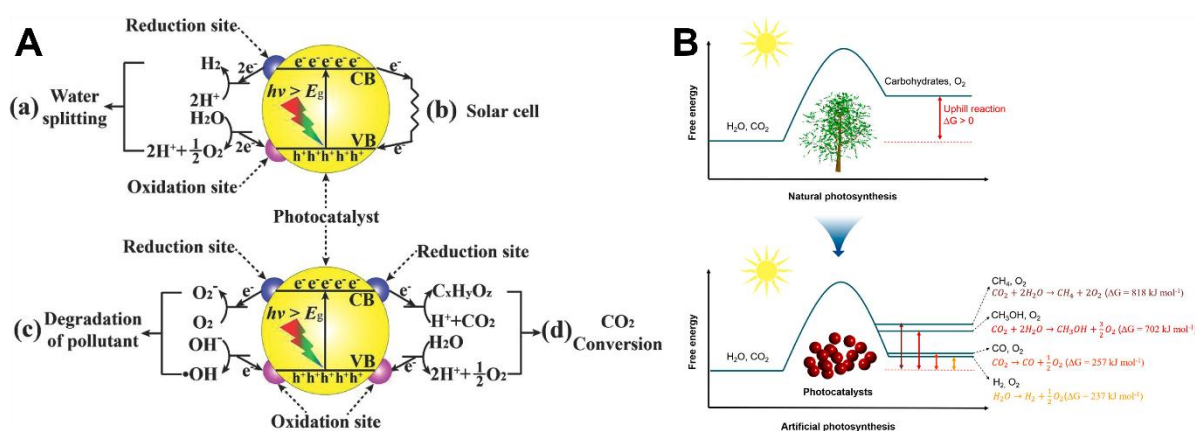
139
 140 **Fig.1.** Yearly scientific publications and patents on **A)** halloysite, **B)** imogolite and **C)**
 141 chrysolite nanotubes. The data displays the last decade (Data from the “Web of
 142 Science”).

143 **2. Semiconductor photocatalysis: General principles and mechanism**

144 Photocatalytic reactions are regarded as one of the most effective methods for
 145 harnessing solar power. In addition to the established techniques of generating solar fuels
 146 by splitting water and reducing carbon dioxide, photocatalysis has found applications
 147 across a wide range of fields [27,67,70–73], varying from pollutant degradation to fine
 148 chemical production (**Fig.2A**) [74].

149 Generally, the photocatalysis downhill thermodynamics (Gibbs free energy change
 150 $\Delta G < 0$) is purely enhanced by the induced reactive oxygen species (ROS) from the
 151 photocatalysts' excitation under light irradiation (**Fig.2B**) [75]. However, the unfavorable

152 photosynthesis reaction ($\Delta G > 0$), an uphill reaction, is primarily determined by
 153 photogenerated holes and electrons characterized by high redox potentials (**Fig.2B**) that
 154 need to be assured by the correct positioning of the conduction and valence bands [76].
 155 From a thermodynamic point of view, photocatalytic degradation is much more feasible
 156 than the challenging artificial photosynthesis processes, such as photocatalytic hydrogen
 157 (H_2) evolution and the production of hydrocarbon fuels from carbon dioxide (CO_2)
 158 reduction.

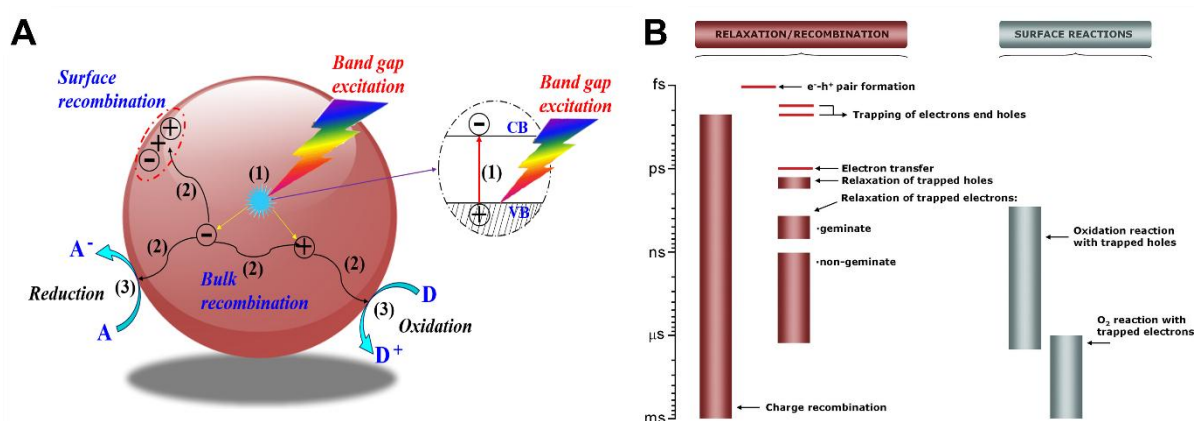


159
 160 **Fig. 2. A)** Water splitting, solar cell, pollutants photocatalytic degradation, and
 161 photocatalytic reduction of CO_2 mechanisms. Adapted with permission from [74],
 162 Copyright (2014), Wiley. **B)** Schematic illustration of natural and artificial
 163 photosynthetic systems [77], Copyright (2019), American Chemical Society.

164
 165 **Fig.3A** displays the redox mechanism for semiconductors (SCs) used as
 166 photocatalysts. The mechanism involves three successive steps [78,79]. Initially, the
 167 SC photocatalyst absorbs photons, and this causes electrons (e^-) in the valence
 168 band (VB) to jump to the conduction band (CB) when the photon energy ($h\nu$)
 169 exceeds the bandgap energy (E_g) of the semiconductor. Consequently, holes (h^+)
 170 are left behind in the VB. These electrons and holes are crucial in driving reduction
 171 and oxidation reactions to yield the desired product [79]. The subsequent step
 172 involves separating and transferring photogenerated electron-hole pairs, directing
 173 them toward the semiconductor's surface, although some of these pairs may

174 recombine within the bulk of the photocatalyst [80]. The last step comprises surface-
 175 based reduction and oxidation reactions. The photogenerated charges located on
 176 the surface of the semiconductor engage with chemical species, thus initiating the
 177 desired chemical reactions. However, on the surface, certain photogenerated
 178 electrons (e^-) and holes (h^+) may recombine without actively engaging in chemical
 179 reactions. **Fig.3B** displays a schematic representation of the time scale
 180 characteristics associated with the various phenomena related to charge carriers that
 181 were previously discussed [81].

182 With the modern insight into the photocatalytic mechanisms, enhancing the
 183 effectiveness of semiconductor photocatalysts involves expediting the production,
 184 mobility, and reactivity of photo-induced charge carriers while minimizing electron-
 185 hole recombination. Semiconductor materials with suitable bandgap structures for
 186 solar light absorption, efficient conductivity for charge transport, minimal defects as
 187 recombination sites, and rapid kinetics for surface reactions are highly favored
 188 [82,83]. In general, for the reaction to proceed effectively, the reduction potential
 189 should be lower than the bottom edge of the semiconductor's conduction band (CB),
 190 enabling the transfer of electrons from the CB to the reactant. Furthermore, the
 191 oxidation potential must exceed the VB of the catalyst to ensure the reactant can
 192 readily accept holes.



193

194 **Fig. 3. A)** Schematic diagram illustrating principle of photocatalyst photocatalysis. **B)**
195 Time intervals between "elementary steps" in a typical photocatalytic reaction.
196 Adapted with permission from [81], Copyright (2012), American Chemical Society.

197

198 Adsorption plays a pivotal role in heterogeneous photocatalysis [84–86],
199 particularly in the degradation and transformation of organic molecules or gases,
200 where clay catalysts have emerged as significant contributors. Clay minerals, with
201 their abundant surface area and reactive sites, offer a favorable environment for
202 adsorption and catalytic processes [50,53,87]. Organic molecules or gas reactants
203 adhere to the surface or interlayer spaces of clay catalysts through electrostatic
204 interactions and other surface phenomena, initiating photocatalytic reactions. The
205 subsequent generation of superoxide and hydroxyl radicals facilitates the breakdown
206 of adsorbed molecules, leading to the desired transformations [88,89]. Despite the
207 essential role of adsorption, competitive interactions among water molecules, other
208 reactants, and target molecules may influence the photocatalytic efficiency,
209 impacting active site availability and photogenerated species migration. While
210 adsorption enhances catalytic efficiency by promoting reactant-catalyst interactions,
211 excessive adsorption of certain compounds or intermediates can impede the process
212 by acting as catalyst poisons [90]. Nonetheless, adsorption serves as the initial step
213 in catalysis, concentrating reactants near active sites, and reducing the activation
214 energy required for chemical transformations to occur. The versatility of clay
215 catalysts allows for tailored surface properties and selective adsorption, enabling the
216 direction of reactions toward desired pathways and improving overall process
217 performance in terms of reaction rates, selectivity, and yield for various organic
218 molecules or gas reactants [89].

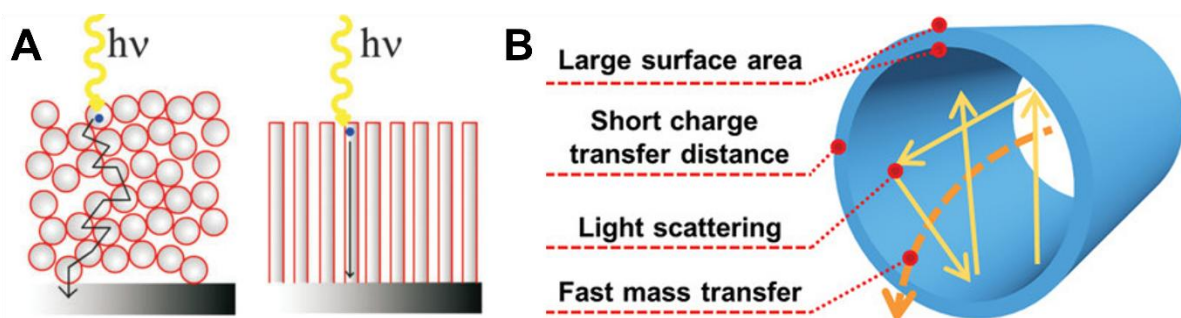
219 Recently, several studies demonstrated that tube morphology is one of the
220 crucial parameters that can significantly influence the performance of the

221 photocatalyst [27,91,92]. In particular, there is compelling evidence that materials
222 featuring nanotubes display improved photocatalytic activity compared to
223 nanoparticles. Moreover, materials with tubular structures have been reported to
224 exhibit much better photocatalytic performance than nanoparticulate systems. For
225 instance, a study by Jiang et al [93] demonstrated that halloysite exhibits superior
226 photocatalytic activity in photodegradation processes of different organic
227 contaminants (rhodamine B, malachite green and ciprofloxacin) compared to their
228 2D polymorph (kaolinite nanosheets). Their results highlight the enhancement of
229 photocatalytic activity due to the tubular morphology of halloysite. The extended axis
230 of nanotube photocatalysts provides a straight path for carrier transport [94], thus
231 lowering photoinduced electron-hole pairs' trapping and recombination kinetics [95].
232 This compares sharply with the transporting of the electron-hole pairs between
233 nanoparticles. Moreover, nanotubes can provide a strong light-scattering effect,
234 improving the light-harvesting properties [94]. Additionally, polarization can improve
235 charge separation within a photocatalyst material by facilitating the movement of
236 electrons and holes in opposite directions [96]. The nanotubes' geometry reduces
237 the diffusion distance between the degrading compounds in the solution and the
238 nanotubes' active surface area. Whereas the porous structure of nanoparticles
239 imparts longer diffusion lengths [95]. These advantages can be applied to nanosized
240 tubular clay minerals (halloysite, imogolite, and chrysotile). **Fig. 4A and Fig. 4B**
241 outline the electron transport in two distinct architectures of the photocatalyst and
242 schematic illustrations of some pros of nanotubular architecture for photocatalytic
243 reaction, respectively.

244 We can summarize and highlight the action mechanism of clay nanotubes in
245 altering photocatalytic properties as follows: The tubular architecture of these clay

246 variants provides a confined environment that boosts the efficiency of photocatalytic
247 reactions by facilitating the adsorption of reactant molecules and promotes proximity
248 to active sites and catalytic centers [93,97]. Additionally, the high surface area-to-
249 volume ratio of clay nanotubes allows for increased contact between catalysts and
250 reactants, enhancing reaction kinetics [93]. Moreover, their structural characteristics
251 enable efficient light harvesting and photon utilization, while surface chemistry
252 facilitates charge transfer processes crucial in photocatalytic reactions [98,99]. The
253 polarization effect within tubular clay minerals further aligns molecules and charge
254 carriers, streamlining charge transfer and reducing recombination rates, thus
255 amplifying overall photocatalytic activity [100,101].

256



257

258 **Fig. 4. A)** A comparison of the electron pathways through nanoparticle and
259 nanotubular structured TiO₂. Reproduced with permission from [102], Copyright
260 (2009). The Royal Society of Chemistry. **B)** Schematic illustration of some
261 advantages of nanotubular architecture for photocatalytic reactions. Reproduced with
262 permission from [103], Copyright (2019) Wiley.

263

264 3. Structural and physiochemical properties of the nanosized tubular 265 clay minerals.

266 Compared to other nanomaterials with spherical or platy shapes, nanotubes,
267 such as chrysotile, halloysite, and imogolite, offer a larger surface area due to their
268 unique hollow tubular structure [104]. In the following discussion, we will examine the
269 detailed aspects of these nanosized tubular clay minerals, exploring their

270 composition, structure, and exceptional physiochemical properties that distinguish
271 them in materials science.

272

273

274 **3.1. Structural and physiochemical properties of Halloysite**

275 Halloysite nanotubes (HNTs) represent an exciting source of 1D clay material
276 that can be extracted in large quantities from deposits, making them economically
277 viable. The most widely available halloysite supplies are from Dragon Mine (Utah-
278 USA) and Northland (New Zealand) deposits [105,106]. Due to its distinctive tubular
279 nanostructure, HNTs has garnered significant attention across various fields in
280 recent years. Its applications range from controlled release of functional compounds,
281 anticorrosion, adsorbents, catalysis supports and nanotemplate/nanoreactor
282 [93,97,107–110].

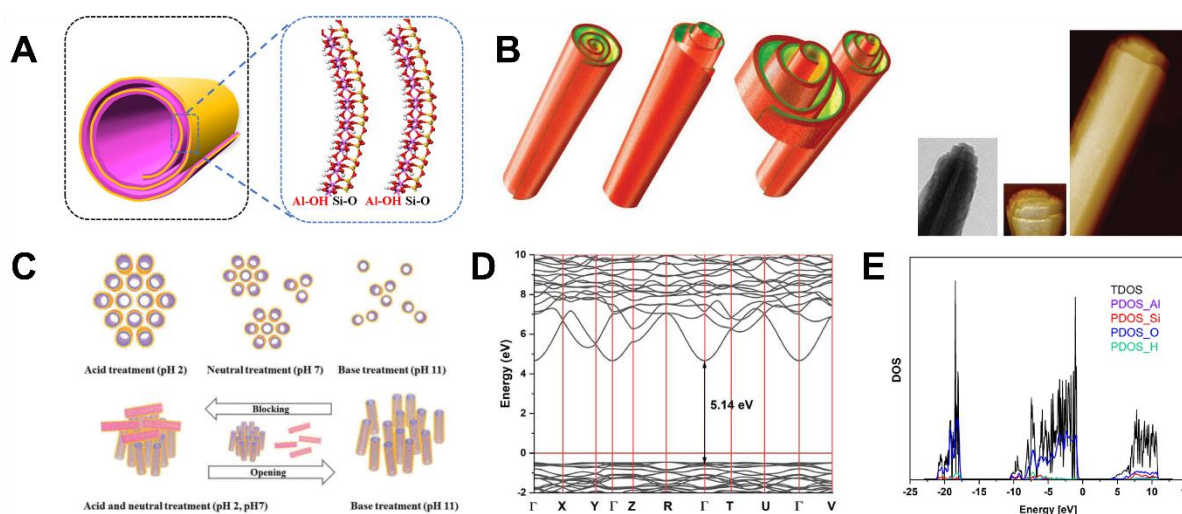
283 Halloysite is a dioctahedral 1:1 clay mineral with a chemical formula of
284 $\text{Al}_2(\text{OH})_4\text{Si}_2\text{O}_5 \cdot n\text{H}_2\text{O}$, belonging to the kaolin group with a nanoscroll shape formed
285 by rolling 5-20 aluminosilicate layers [111,112] (**Fig. 5A**). When $n = 2$, halloysite is
286 referred to as halloysite-10 Å due to the average spacing of 10 Å between the unit
287 layers. Water can be removed almost permanently by heating the halloysite samples
288 at 120 °C, leading to halloysite-7 Å (with an interlayer spacing of 7Å) [87]. The
289 structure of halloysite is known as monoclinic with unit cell parameters as follows: a
290 = 5.14, $b = 8.9$, $c = 17.7$ Å with angles α ranging from 97 to 104 degrees, β from 90
291 to 91.8 degrees, and γ fixed at 90 degrees. The halloysite is characterized by a
292 hollow spiral structure [113] as illustrated by images using AFM and TEM techniques
293 (**Fig. 5B**). The length of HNTs ranges typically within 0.5-1.5 μm [111,112]. The outer

294 diameter ranges between 50 to 70 nm, while the inner cavity, also called lumen, has
295 a 10 to 20 nm diameter. In addition, halloysite exhibits distinct internal and external
296 chemistry. The inner lumen surface features an array of Al-OH groups resembling
297 gibbsite and carries a positive charge, whereas the outer surface consists of
298 Si-O-Si groups and bears a negative charge [41]. This characteristic of a different
299 surface charge outside and inside the tube makes the incorporation of ligands and
300 nanomaterials feasible in the desired location. Joo *et al.* [114] observed that
301 changing the pH in a water suspension containing HNTs allowed the tailoring of the
302 pore surface area, pore diameter, and pore volume of the recovered halloysite
303 powder (**Fig. 5C**). Indeed, in an acidic solution, bundles of halloysite nanotubes are
304 formed (blocking the halloysite nanotube inner pore). In contrast, HNTs are well
305 dispersed in basic solution, and the end of each HNTs was separated from other
306 HNTs. An important point it that the synthesis of halloysite remains an ongoing
307 challenge due to the absence of well-established procedures. Research efforts in
308 this area have been underway since the mid-20th century. However, to date,
309 developing a reliable and efficient method for synthesizing halloysite in the laboratory
310 continues to be an urgent and unresolved issue [115].

311 Continuing the research on the properties of the HNTs, Gianni et al [116].
312 conducted a comprehensive theoretical study using DFT calculations to examine the
313 electronic characteristics of halloysite nanotube models (**Fig. 5D**). Their study
314 revealed that the pristine halloysite nanotube exhibits a band gap of 5.14 eV (**Fig.**
315 **5E**). Through the analysis of the total density of states (TDOS) and projected density
316 of states (PDOS) of halloysite, they highlighted that the lower and upper sections of
317 the valence band consist primarily of oxygen 2s and oxygen 2p states, respectively.
318 The oxygen atoms forming Al-O bonds significantly contribute to the valence band

319 compared to those involved in Si-O bonds [116,117]. The conduction band minimum
 320 primarily comprises H 1s, Si 3s 3p, and partly O 2p, Al 3s 3p states. The same
 321 calculations were confirmed by independent researchers [116,117].

322 The hollow structure of HNT acts as a nanoreactor, providing a confined
 323 environment that enhances the effectiveness of catalysts. Recently, Jiang and
 324 colleagues [93] investigated the use of natural HNT as a nanoreactor to improve
 325 photochemical reactions. Their research demonstrated that introducing Fe doping
 326 into the interior surface of HNT resulted in enhanced activity and adsorption
 327 capabilities compared to the exterior surface. Notably, the unique photochemical
 328 properties exhibited by the two surfaces of HNT led to spatial confinement effects,
 329 resulting in superior photodegradation of organic species compared to kaolinite
 330 nanosheets.



331
 332 **Fig. 5.** **A)** Detailed structure of halloysite nanotubes. Reproduced with permission
 333 [93]. Copyright (2021), American Chemical Society. **B)** Scheme of the rolling of
 334 aluminosilicate sheets to create halloysite nanotubes, with alumina forming on the
 335 interior (green), silica on the outside and representative TEM and AFM images of
 336 HNTs. Reproduced with permission from [41]. Copyright (2015), Wiley. **C)** Schematic
 337 representation of the inner space of halloysite nanotubes and the inter-space
 338 between them following treatment with various pH solutions. Reproduced with
 339 permission from [114], Copyright (2013), Royal Society of Chemistry. **D)** The
 340 calculated band gaps for and **E):** The calculated TDOS and PDOS of respective

341 atoms for the the halloysite. Reproduced with permission from [116] Copyright
342 (2023), Elsevier.

343

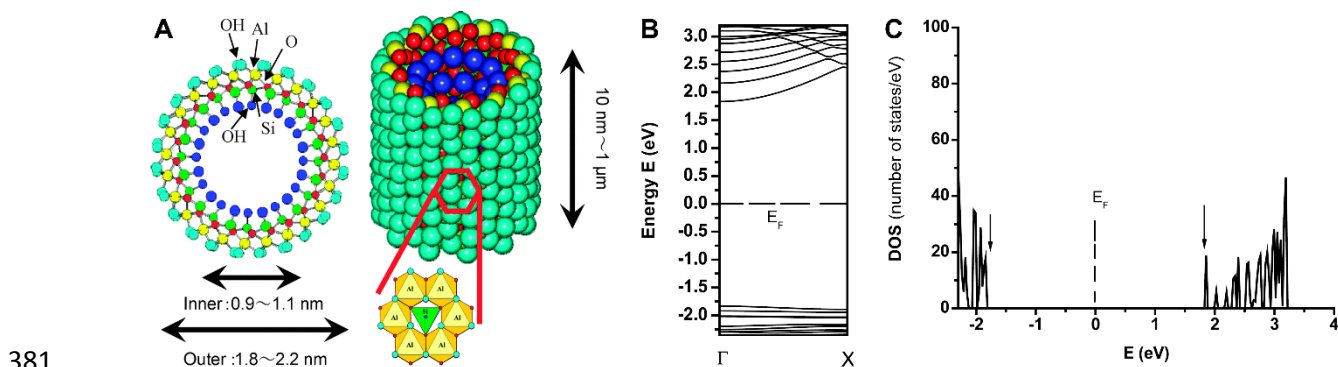
344 **3.2. Structural and physiochemical properties of imogolite**

345 Yoshinaga and Aomine first discovered imogolite (INT) from volcanic ash in
346 1962. INT is a naturally occurring aluminosilicate nanotube [118], characterized by
347 the chemical formula $(\text{OH})_3\text{Al}_2\text{O}_3\text{SiOH}$, extending from the outer to the inner surface
348 of these nanotubes [53,119]. This particular nanotube features an inner and outer
349 diameter of about 1.0 nanometers and approximately 2 nanometers, respectively
350 [54], while the length varies from hundreds of nanometres to the micrometer scale
351 **(Fig. 6A)**. The interior of imogolite exhibits silanol (SiOH) groups, while the exterior
352 showcases both Al–O–Al and Al–OH–Al groups, providing imogolite nanotubes with
353 amphoteric properties [120]. The spontaneous rolling of an Al–O and Si–O bond into
354 a single-walled nanotube is caused by the difference in bond length. More
355 interestingly, these configurations exhibit a clearly defined minimum in strain energy
356 [57,58,121], facilitating monodispersity in nanotube diameter and chirality [122]. It is
357 worth highlighting that the structure of imogolite differs significantly from that of
358 halloysite. In imogolite, the curved octahedral $[\text{Al}(\text{OH})_3]$ layer shapes the inner
359 surface of the nanotubes, whereas the outer surface is composed by Si–O–Si group
360 [53]. These distinctions are at the core of the unique characteristics of imogolite
361 nanotubes. Moreover, INTs are often regarded as the clay equivalent of carbon
362 nanotubes, exhibiting remarkable resemblances in aspect ratios, rigidity, and
363 dimensions [112].

364 The major limitation of INTs, from an industrial point of view, is their inability to
365 create extensive deposits [123]. However, its synthesis was established quite rapidly
366 after its discovery. In 1977, for the first time, Farmer et al. [124] synthesized

367 imogolite nanotubes by coprecipitating silicon and aluminum in an aqueous solution.
368 They established that the yield and rate of formation of imogolite nanotubes are
369 optimal for (i) a pH of 4.5, (ii) low reactant concentrations, and (iii) a temperature
370 between 90 and 100 °C [125].

371 The electronic characteristics of INTs depend on their diameter, chemical
372 composition, and chirality. An indicator of a promising photocatalyst is its band gap.
373 Bursill et al. [126] were the first to predict a relatively wide band gap for these
374 nanotubes. Subsequent band gap values for imogolite nanotubes have been shown
375 to range from 3.6 to 5.3 eV [57,58,64,127,128]. Moreover, Li and co-workers [127]
376 demonstrated that the structure of the energy band and the electron density of states
377 were near the Fermi level (set at $E=0$) for a single-walled imogolite (**Fig. 6B**). Their
378 findings indicated a direct band gap with an E_g of approximately 3.67 eV. Moreover,
379 the energy gap shown in the DOS (**Fig. 6B**) corresponds to the energy band gap
380 shown in **Fig. 6C**.



382 **Fig. 6. A)** Structural illustration of imogolite. Reproduced with permission from [129],
383 Copyright (2014), Royal Society of Chemistry. **B)** The energy bands of the single-
384 walled imogolite nanotube and **C)** the electron density of states. Reproduced with
385 permission from [127]. Copyright (2008), IOP Publishing.

386

387 3.2.1. Synthesis and physiochemical properties of compounds

388 analogous to imogolites

389 Chemically tuning synthetic materials primarily aims to expand the range of
390 potential industrial applications. Similarly, synthetic procedures often allow for better
391 control over reproducibility, composition, purity, and specific desired characteristics,
392 unlike natural clay specimens, which frequently contain impurities and can be less
393 readily available. Notably, in the case of nanotubular structures, it is essential to
394 establish practical approaches for controlling the functionality of both their inner and
395 outer surfaces.

396 Wada and co-workers successfully substituted the silicon atoms with
397 germanium in the imogolite structure by modifying the precursors of the synthesis
398 [130]: By using electron microscopy and X-ray scattering analysis, they found that
399 the diameter of imogolite nanotubes increases as the $[Ge]/([Ge]+[Si])$ ratio increases.
400 Conversely, they also observed a reduction in the length of the tubes with the
401 increase in this substitution rate. It's worth mentioning that by replacing NaOH with
402 urea in the synthesis procedure, some researchers substantially increased the length
403 of Ge tubes [131,132]. However, Maillet et al. [133] observed in their study that the
404 nanotube shape is regulated by the initial aluminum salt (C_{Al}) concentration,
405 generating either single-walled nanotubes (Ge-SWINT, $C_{Al} > 0.75 \text{ mol L}^{-1}$) or double-
406 walled (Ge-DWINT, $C_{Al} < 0.4 \text{ mol L}^{-1}$) (**Fig. 7A**) [53]. These structures (Ge-SWINT
407 and Ge-DWINT) have been thoroughly investigated through experimental and
408 computational studies [65]. The results of this study proved that the Ge-DWINT
409 structure exhibits more excellent stability compared to Ge-SWINT, possibly
410 attributable to hydrogen bonding stabilization. It has also been deduced that while
411 aluminosilicate nanotubes exhibit insulating properties, their dehydroxylation can
412 alter them into semiconductor materials [133]. On the other hand, Alvarez-Ramirez

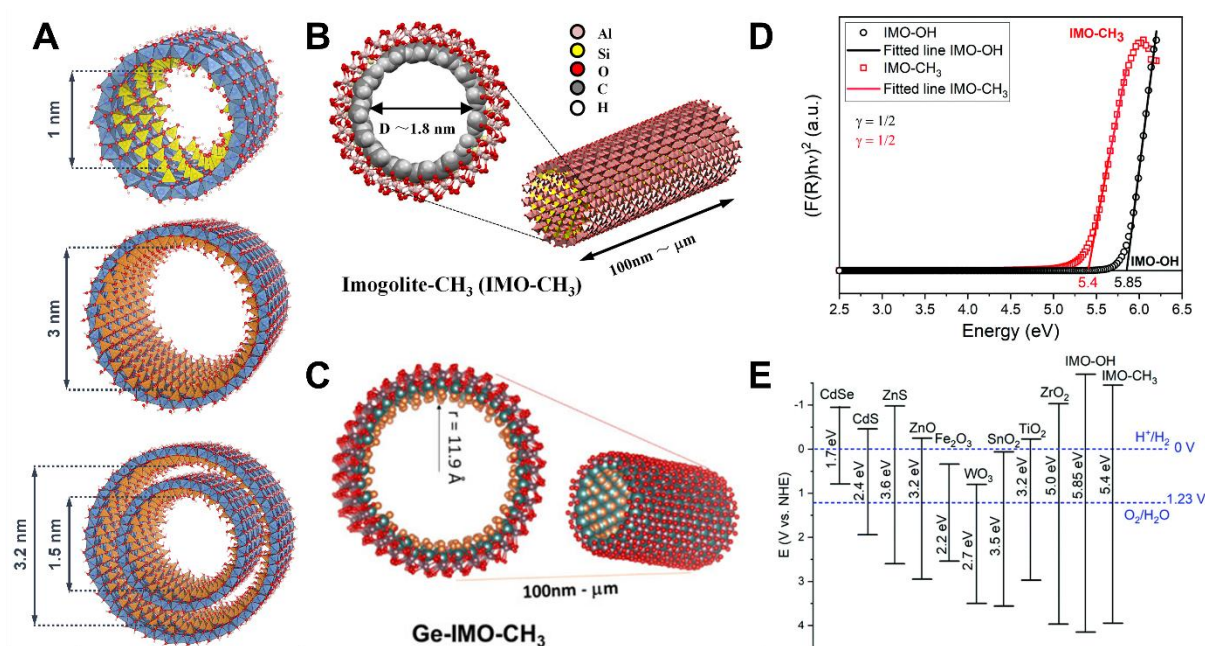
413 [128] performed ab initio simulations, from which they estimated a band gap range of
414 4.3-4.8 eV for Ge-Imo.

415 Surface modification has also been applied to Imogolite nanotubes. Bottero et
416 al. [134] were the first to report the synthesis of silicon-based imogolite with a fully
417 methylated inner wall (**Fig. 7B**) [135]. A few years later, the technique was
418 successfully transposed to germanium imogolite nanotubes (**Fig. 7C**) [136,137]. It
419 was worth mentioning that the methylation of imogolite nanotubes was confirmed to
420 induce a significant increase in their affinity with molecules such as CH₄, CO₂, or N₂
421 [138]. Curiously, Pignié et al. [100] recently reported that the imogolite IMO-CH₃ (5.4
422 ± 0.2) has a smaller energy gap than the pure imogolite IMO-OH (5.85 ± 0.30) (**Fig.**
423 **7D**). This value is similar to the band gap related to ZrO₂ (**Fig. 7E**), whose
424 photocatalytic activity has been extensively studied. Given the similarity in band gaps
425 and valence/conduction bands between ZnO₂ and imogolite variants (IMO-CH₃ and
426 MO-OH) [100] and the successful use of ZnO₂ in harnessing solar energy [139–141],
427 it suggests imogolite holds promise as a viable candidate for effective photocatalytic
428 applications. Furthermore, the versatility of imogolite nanotube functionalization
429 opens exciting opportunities in the field of photocatalysis.

430 Finally, focused on these encouraging findings, other isomorphous substitutions
431 have been studied lately, especially regarding the partial replacement of Al³⁺ with
432 Fe³⁺ in the outer wall [142–144]. Despite these enhancements, they do not
433 substantially alter the nanotube diameter, with doping rates remaining below 1%
434 [142]. Alvarez-Ramírez's work has shown that the incorporation of Fe alters the
435 electronic characteristics of the nanotubes, consequently causing the band gap
436 value to decrease. This decrease is observed from 4.7 eV to 2.0-1.4 eV for the Fe-
437 silicon nanotubes and from 4.2 eV to 2.6-1.0 eV for the Fe-germanium imogolite-like

438 nanotube [63]. "In addition to iron substitution, other trivalent dopants or cation
 439 vacancies have been theoretically contemplated, which have the potential to bring
 440 about substantial alterations in the band structure of these nanotubes [145–148].
 441 Therefore, these different perspectives on the optical and electronic properties of
 442 modified imogolite nanotubes open the way to their practical use as a photochemical
 443 nano-reactor.

444



445

446 **Fig. 7.** Inner diameter size for **A**) Si-SWINT, Ge-SWINT and Ge-DWINT.
 447 Reproduced with permission from [53], Copyright (2018) MDPI. **B**) Methylated
 448 imogolite (IMO-CH₃). Reproduced with permission from [137], Copyright (2017)
 449 Elsevier. **C**) SW Ge-IMO-CH₃. Reproduced with permission from [135], Copyright
 450 (2019) American Chemical Society. **D**) Band gap energy of IMO-OH and IMO-CH₃
 451 and **E**) Comparison of the gap band of the imogolite with other selected compounds.
 452 Reproduced with permission from [100], Copyright (2021) Royal Society of
 453 Chemistry.

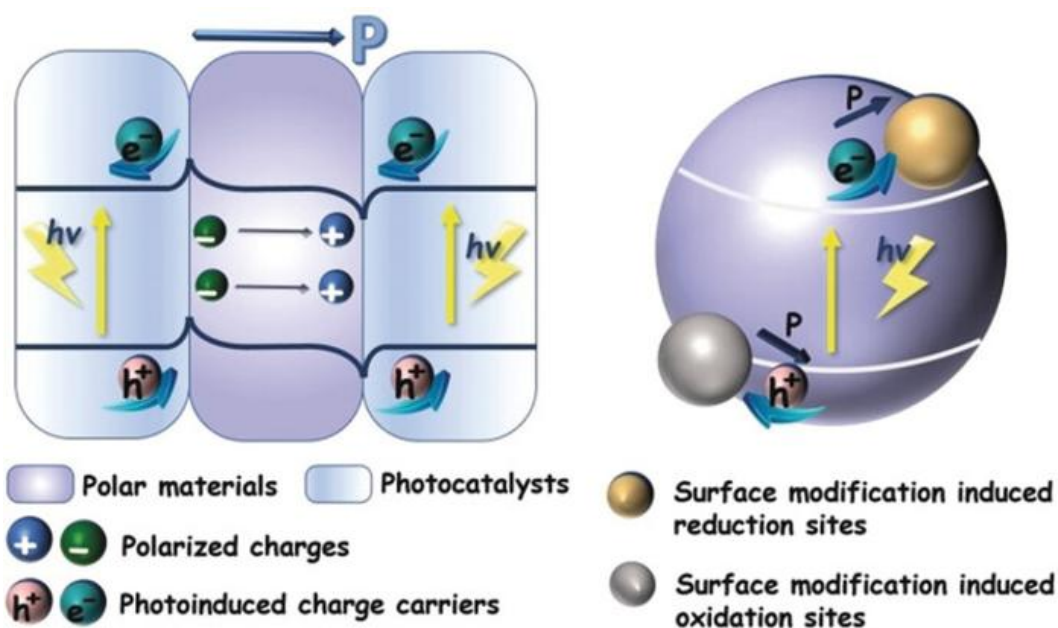
454

455 3.2.2. The role of polarization of imogolite in photocatalysis

456 As mentioned, a fundamental challenge in photocatalysis lies in rapidly
 457 recombining electron-hole pairs within photocatalysts. While the charge migration

458 requires hundreds of ps, bulk charge recombination occurs much faster, taking only
459 a few ps. which is considerably swifter than charge transport [149]. For that reason,
460 Therefore, suppressing the process of electron-hole pairs recombining (e^-/h^+) stands
461 as a crucial factor in improving the performance of photocatalysts. The electric field
462 inside the substance induces a static force on the charges in the opposite direction,
463 which makes it possible to increase their lifetime by limiting their recombination
464 [101]. This electric field also promotes their transport to the interfaces where the
465 chemical reactions of interest occur (**Fig. 8**). Discussions regarding the potential role
466 of persistent polarizations in facilitating efficient separation of electrons (e^-) and holes
467 (h^+) have started to appear in the literature [150–152].

468 However, it is essential to note that in the case of imogolite, the nanotube
469 serves a unique dual role, acting as both a polar material and a photocatalyst,
470 distinguishing it from the scenario presented here [53,65,100,119]. The inherent
471 polarization of imogolite nanotubes, coupled with their photocatalytic activity, creates
472 a synergetic effect that significantly enhances their performance in light-driven
473 catalytic reactions. This dual functionality showcases how imogolite seamlessly
474 integrates both the roles of a polar medium and a photocatalyst, offering a unique
475 and promising platform for efficient photoinduced catalysis, where the material's
476 polar nature finely tunes charge separation and transport.



477

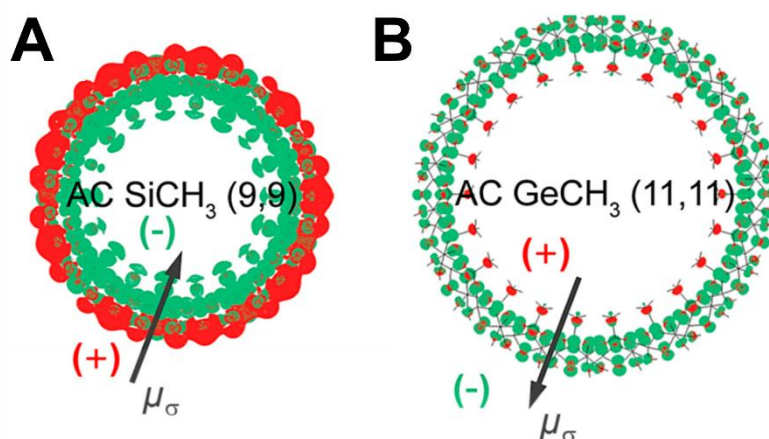
478 **Fig. 8.** The scheme for polarization promoted surface charge separation.
 479 Reproduced with permission from [101] .Copyright (2019), Wiley.

480

481 In this context, Gustafsson and co-workers first discussed the intrinsic
 482 polarization in natural imogolite in 2001 [153]. They explained that the pKa of the
 483 hydroxyl functions that compose the inner and outer surfaces could not justify the
 484 evolution of the charge of the outer surface of INTs as a function of pH. In general, in
 485 aluminum oxides, the aluminol functions, similar to imogolite, remain uncharged over
 486 a broad pH range, from 0 to 11.9 [153]. Moreover, surface complexation of ions by
 487 these groups is not considered possible. Consequently, they assumed that the outer
 488 tube walls are unreactive toward ions. The authors, therefore, proposed a model in
 489 which negative and positive charges accumulate on the internal and external
 490 surfaces of the nanotube, respectively. These charges are not dependent on the pH.
 491 They thus defended the existence of polarization through the wall.

492 Teobaldi's group conducted density functional theory (DFT) calculations
 493 concerning INTs, focusing on various physico-chemical structures [57,154]. These
 494 simulations have shown that INTs exhibit a persistent polarization corresponding to a

495 spatial separation of the VB and CB in real space (**Fig. 9**) [57,154]. This separation
496 enhances the separation of holes (h^+) and electrons (e^-) through optical charge-
497 transfer excitations inside the walls of the nanotubes.



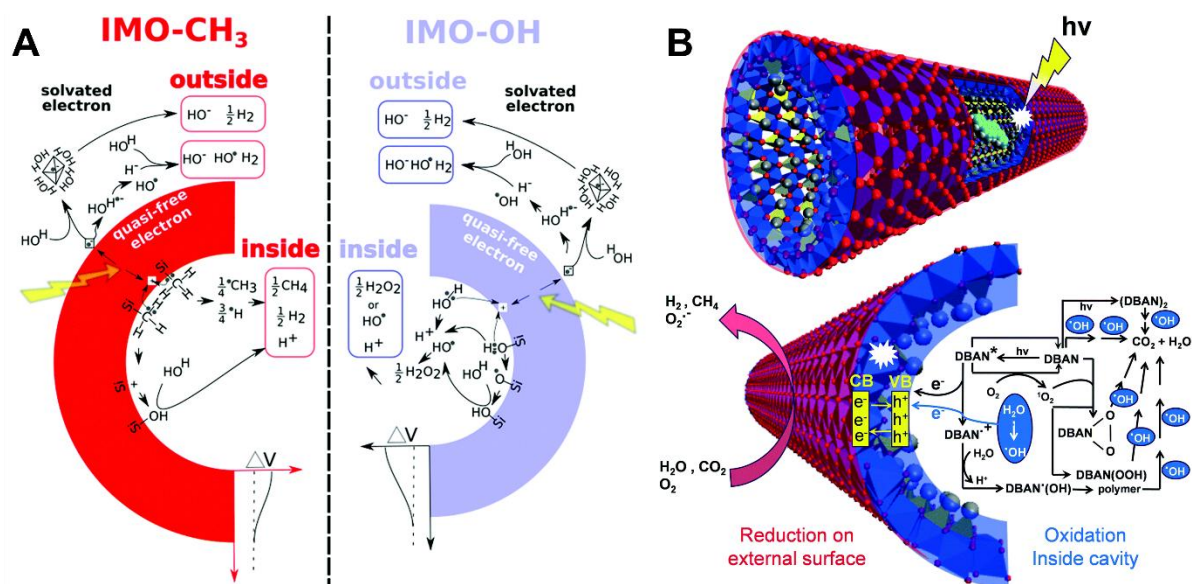
498

499 **Fig. 9.** Front image of armchair methylated INTs $(OH)_3Al_2O_3Y(CH_3)$ showing the real-
500 space separation between the boundaries of the conduction band (red) and valence
501 band (green). $Y = Si$ in (A) and Ge in (B). The direction of the permanent dipole
502 surface density μ_σ of the nanotube wall is indicated by the black arrow. Reproduced
503 with permission from [122], Copyright (2018) Nature.

504

505 Furthermore, the excellent chemical separation characteristics of hybrid
506 hydrophobic/hydrophilic Imo NTs, along with their ease of modification
507 [136,138,155,156] could be very favorable for the effective separation of photo-
508 oxidized and photo-reduced reactants and products (**Fig. 10A** and **Fig. 10B**). Articles
509 discussing the potential beneficial impact of permanent polarizations on the effective
510 separation of holes (h^+) and electrons (e^-) have started to appear in the literature
511 [65,100,154,157], prompting increasing interest in this field.

512 Although INTs have been utilized as catalyst supports (as discussed in
513 section 4) and initial findings have been reported regarding their efficacy in the
514 photocatalytic decomposition of organic dyes [40,97,98], this subject is yet to be
515 explored.



516

517 **Fig. 10. A)** Schematic of the reaction mechanisms at play in two types of
 518 imogolites (IMO-CH₃ and IMO-OH). For clarity, water radiolysis was left out. The
 519 intra-wall electric field (ΔV), which drives charge separation, is schematically
 520 represented. Reproduced with permission from [66], Copyright (2021) The Royal
 521 Society of Chemistry. **B)** Illustration of potential key photodegradation pathways for
 522 DBAN enclosed in Imo-CH₃ nanotubes in an aqueous medium. Reproduced with
 523 permission from [96], Copyright (2021) The Royal Society of Chemistry.

524

525

526 3.3. Structural and physiochemical properties of chrysotile

527 Chrysolite is a hydrated magnesium silicate with a stoichiometric composition
 528 of Mg₃Si₂O₅(OH)₄. Natural chrysotile, commonly known as white asbestos [158,159],
 529 is part of the serpentine group of minerals. It has found extensive applications across
 530 diverse industries thanks to its remarkable properties, including high tensile strength,
 531 flexibility, and excellent resistance to heat and chemicals. However, despite its
 532 extensive use, there are growing concerns about the potential health risks of
 533 exposure to chrysotile fibers. Inhalation of these tiny fibers can result in severe
 534 respiratory problems, including lung diseases like asbestosis and mesothelioma,
 535 which is a rare and aggressive form of cancer [159–161].

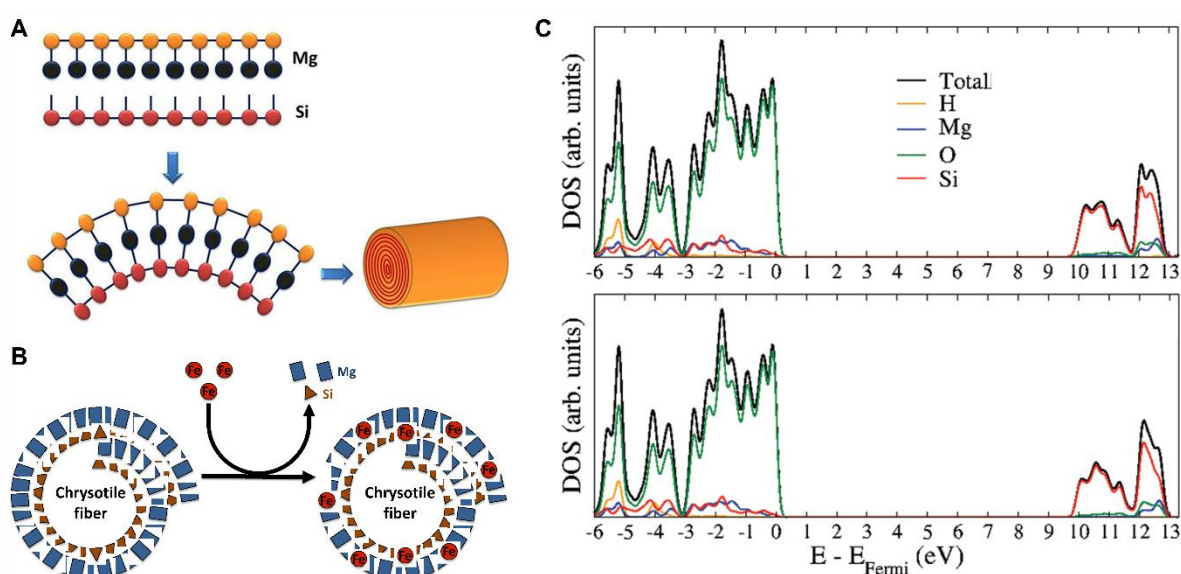
536 Chrysotile consists of a silicate sheet $(\text{Si}_2\text{O}_5)_n^{2n-}$, where the neighboring
537 tetrahedra share the oxygen atoms present in the tetrahedron, and a non-silicate
538 sheet $[\text{Mg}_3\text{O}_2(\text{OH})_4]_n^{2n+}$ [162]. The curvature of the sheets spreads along a favored
539 axis, giving rise to the tubular chrysotile structure similar to that seen for halloysite
540 **(Fig. 11A)**. The concentric sheets developing the fibers exhibit a curvature radius
541 ranging from 2.5 to 3.0 nanometers for the inner layers, expanding to approximately
542 25 nanometers for the outer layers. As a result, unit fibers (fibrils) have external
543 diameters that vary between 20 and 50 nanometers [163]. Researchers have tried to
544 refine chrysotile's structure through the Rietveld method. In a study conducted by
545 Falini et al. [164], they refined nano-chrysotile within the monoclinic Cc space group,
546 determining lattice constants $a=5.340(1)$, $b=9.241(1)$, $c=14.689(2)$ Å, and $\beta=93.66$
547 $(3)^\circ$ [165]. The chemical composition of chrysotile differs depending on the mineral
548 deposit. In fact, the substitution of silicon and magnesium can occur in chrysotile. In
549 the brucite layer, it is possible to substitute magnesium with Mn^{2+} , Fe^{2+} , or Ni^{2+} [166].
550 Conversely, in the silicate layer, silicon can be replaced by Al^{3+} or rarely Fe^{3+} [167]
551 **(Fig. 11B)**.

552 Chrysotile exhibits chemical stability, incombustibility, and exceptional thermal
553 insulation properties [168]. Additionally, its fibrils are known for their strength and
554 remarkable flexibility. These fibers exhibit low thermal conductivity (0.3-0.4 W/(m K)),
555 exceptional ability to withstand high temperatures, and a high melting point
556 (approximately 1500 °C). They possess greater rigidity compared to steel, are
557 impressive, resistant to corrosion, and not expensive compared to synthetic fibers
558 [169].

559 The investigation conducted by Lourenço et al [171]. on the electronic
560 properties of Single-Walled Chrysotile Nanotubes (NTs) using the self-consistent

561 charge density-functional tight-binding method (SCC-DFTB) sheds light on the
 562 intricate electronic structure of chrysotile. Their findings reveal intriguing insights into
 563 the total (DOS) and partial density of states (PDOS) of zigzag (40,0) and armchair
 564 (25,25) chrysotile NTs (**Fig. 11C**). Surprisingly, they discovered that the chirality and
 565 size of the NTs do not significantly alter their electronic structure, as evidenced by
 566 the similarity in DOS and PDOS profiles (Figure 5). Specifically, in the valence band,
 567 the predominant states are attributed to oxygen atoms, while in the conduction band,
 568 electronic states of silicon atoms play a pivotal role in shaping the total DOS.
 569 Interestingly, the contribution of magnesium and hydrogen atoms to the total DOS is
 570 comparatively smaller than that of silicon and oxygen in both valence and conduction
 571 bands.

572



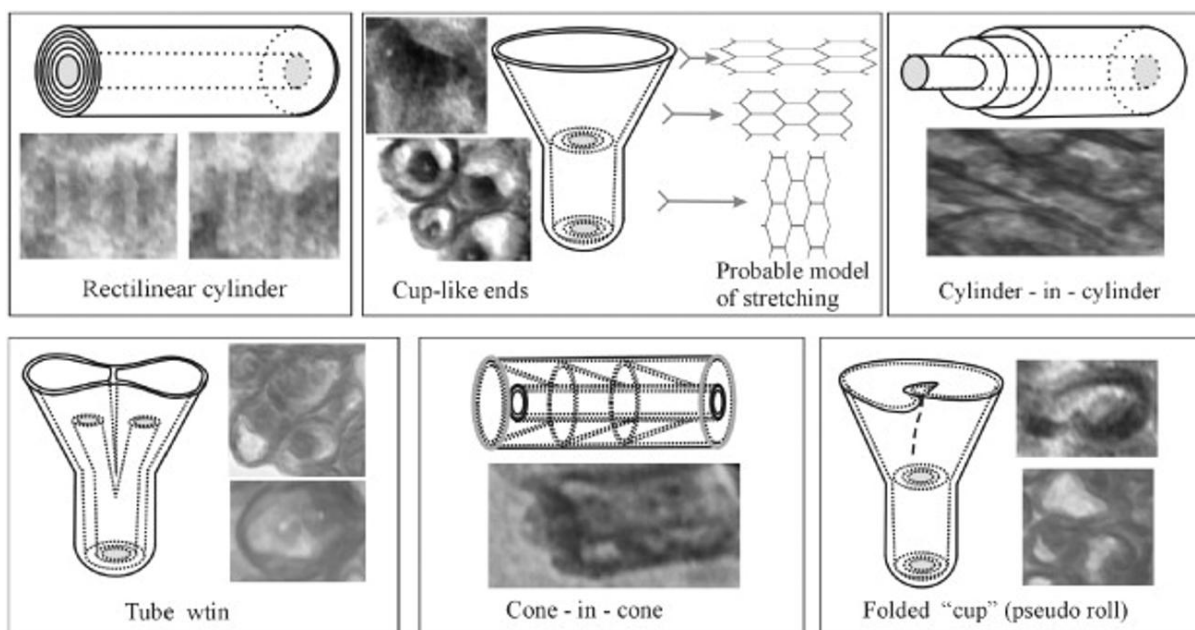
573

574 **Fig. 11.** **A)** structure of chrysotile. Reproduced with permission from [170], Copyright
 575 (2013) Scientific research. **B)** Depiction of magnesium and silicon substitution by iron
 576 in the chrysotile fiber structure. Reproduced with permission from [167], Copyright
 577 (2020) MDPI. **C)** Total and partial density of states (PDOS) of the (a) zigzag (40,0)
 578 and (b) armchair (25,25) chrysotile nanotubes. Reproduced with permission from
 579 [171], Copyright (2012), American Chemical Society.

580

581 An electron-microscopic study of chrysotile by Voitylov et al. showed diverse
582 morphologies of nanotubes: cones, cylinders, and socket tubes (**Fig. 12**). Conical
583 nanotubes exhibit external diameters between 20 and 50 nm, while cylindrical
584 nanotubes have external diameters between 20 and 70 nm. The inner diameter of
585 cylindrical nanotubes is 35 nm. Notably, various other forms of chrysotile can also be
586 found in nature (e.g., cylinder-in-cylinder, tube twins, rectilinear cylinders, cone-in-
587 cone tubes, and cylinders with cup-like ends) [169]. It was revealed that synthesis
588 conditions, including factors like temperature, hydrothermal treatment duration, and
589 the composition of the precursor solution, influence specific morphological
590 characteristics of the nanotubes [172].

591 Chrysotile has attracted significant attention due to its catalytic activity. The
592 abundance of active sites and its high surface area make chrysotile-based catalysts
593 highly promising for various chemical reactions [173]. These catalysts have
594 demonstrated remarkable efficiency in numerous processes, such as polymerization,
595 hydrolysis, reduction, and oxidation [174–177], making them versatile tools for
596 organic synthesis and industrial applications. The distinctive fibrous morphology of
597 chrysotile nanotubes creates an environment conducive to catalytic reactions,
598 leading to improved selectivity and reaction kinetics.



599

600 **Fig. 12.** The hypothetical models of the chrysotile nanotubes. Reproduced
 601 with permission from [169], Copyright (2011) Elsevier.

602

603 **4. Applications in photocatalysis**

604 In the realm of photocatalysis, the interface interaction between tubular clay
 605 carriers and active components emerges as a pivotal determinant of performance
 606 and efficacy. Photocatalysis relies on the intricate interplay between light-absorbing
 607 materials and catalytic species to drive chemical transformations for environmental
 608 remediation and energy conversion [178,179]. Within this context, the interface
 609 interaction orchestrates the spatial arrangement, charge transfer dynamics, and
 610 surface chemistry crucial for photogenerated charge carrier migration and surface
 611 redox reactions [178–180]. Physical adsorption of photocatalytic species onto the
 612 tubular clay surfaces establishes localized reaction sites, amplifying photon capture
 613 efficiency and catalytic activity [180–184]. Chemical bonding between the active
 614 components and the clay matrices bolsters stability, mitigates photocorrosion, and
 615 prolongs catalyst lifespan under harsh irradiation conditions. Electrostatic

616 interactions, in turn, regulate the distribution and orientation of photoactive species,
617 optimizing interfacial charge transfer processes and redox kinetics [180–185].
618 Surface coordination phenomena further fine-tune the electronic structure and
619 surface reactivity of the catalyst, tailoring its performance to specific photocatalytic
620 applications [181–185].

621 Due to clay's excellent structural properties and surface areas, nanotubes
622 (chrysotile, halloysite, and imogolite) can be used as a catalyst or co-catalyst in
623 photocatalytic systems. This section summarizes the application of clay nanotubes in
624 photocatalysis from four aspects: Pollutant degradation in the water and air,
625 photocatalytic hydrogen evolution reactions, disinfection of bacteria, and
626 photocatalytic nitrogen fixation.

627 **4.1. Degradation of organic pollutants by photocatalysis**

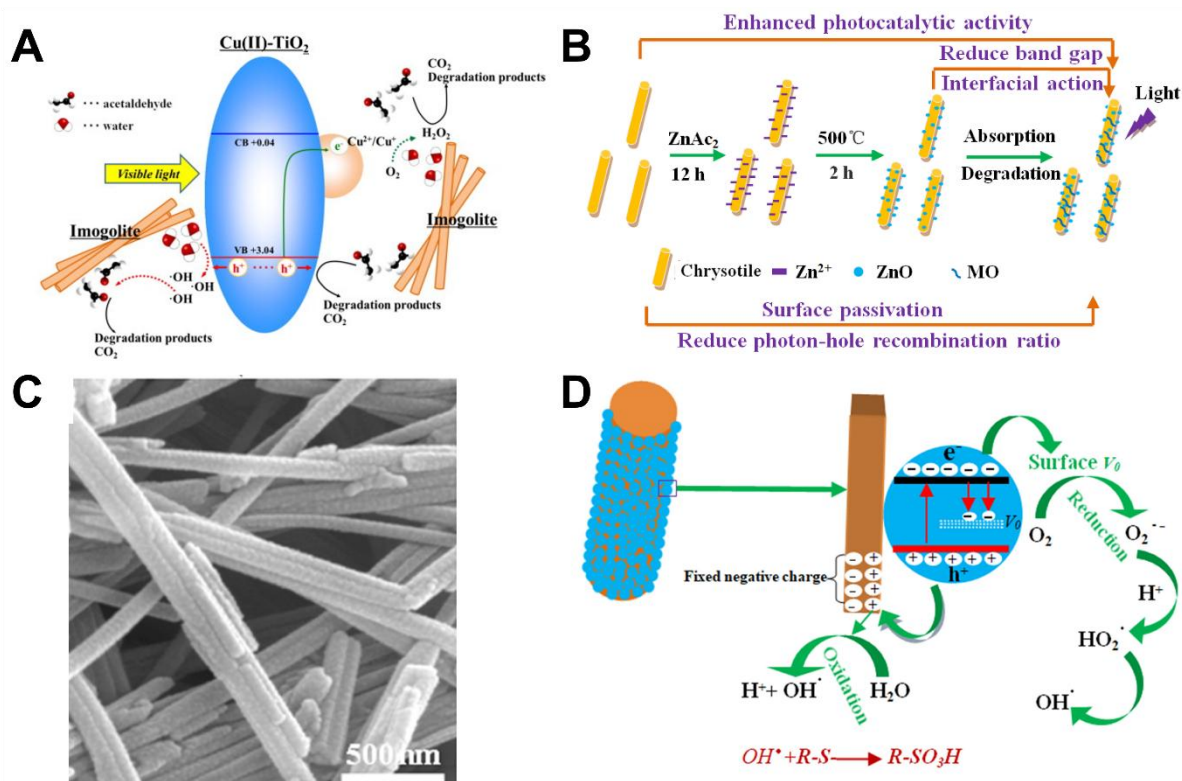
628 With the development of modern industry, a wide range of toxic pollutants,
629 including synthetic dyes, phenol, and pharmaceutical substances, have been
630 discharged into the air, water, and soil, resulting in substantial harm to the
631 environment and living organisms. Thus, various approaches, including chemical
632 degradation, physical adsorption, and biodegradation methods, have been employed
633 for environmental restoration [186–193]. However, many traditional approaches to
634 environmental remediation were deemed ineffective and had the potential to result in
635 secondary pollution. In recent years, solar-driven photocatalysis technology has
636 emerged as an environmentally friendly, efficient, and cost-effective solution for
637 addressing environmental pollution removal. Due to their excellent structural
638 properties and surface areas, clay nanotubes have been attractive candidates for
639 utilizing eco-friendly waste treatment in air and water environments.

640 For instance, Katsumata et al [67]. successfully crafted a nanotubular
641 imogolite structure through a hydrothermal process, subsequently employing it to
642 fabricate composites of imogolite/TiO₂ and imogolite/Cu(II)-grafted TiO₂ (**Fig, 13A**).
643 The authors reported that, under visible light illumination, the composite
644 imogolite/Cu(II)-grafted TiO₂ demonstrated a notable improvement in its efficiency for
645 the photodegradation of acetaldehyde when compared to both TiO₂ and Cu(II)-
646 grafted TiO₂. Furthermore, this enhanced activity appeared less influenced by the
647 relative humidity. This result suggests a unique role of imogolite in effectively
648 adsorbing acetaldehyde. The researchers found that imogolite adsorbs acetaldehyde
649 and captures intermediates, including CH₃COOH, during the acetaldehyde
650 decomposition process. These intermediates are subsequently degraded to CO₂
651 through the action of radical species generated on the catalyst surface. The authors
652 suggested the imogolite-containing composite as a highly efficient photocatalyst and
653 could utterly eliminate the VOCs [67].

654 Similarly, Liu et al. [45] created a novel chrysotile@ZnO nanocomposite by
655 coating ZnO on the surface of chrysotile, as illustrated in (**Fig 13B**). The
656 photocatalytic performance of the chrysotile@ZnO nanocomposite was evaluated
657 under UV light irradiation (365 nm), focusing on its capability for the photocatalytic
658 decomposition of methylene blue (MB) dye. It has been stated that ZnO
659 nanoparticles are homogeneously distributed across the chrysotile surface (**Fig,**
660 **13C**). The team achieved up to 99.5% MB dye degradation after 60 min illumination
661 compared with only 76% obtained with the ZnO, showing that the composite
662 displayed improved light absorption and charge transport. Furthermore, it showcased
663 a capacity for efficient recycling, retaining effectiveness even during the third cycle.
664 The bandgap and photon-hole recombination rate of ZnO nanoparticles are lowered

665 by the combined effects of surface passivation and chrysotile's interfacial action. This
 666 improvement results in enhanced photodegradation of organic pollutants, introducing
 667 a new level of performance to chrysotile (**Fig, 13D**).

668



669

670 **Fig. 13. A)** Cu(II)-grafted TiO₂-imogolite composite: Potential photodegradation
 671 mechanisms of acetaldehyde under visible light irradiation. Reproduced with
 672 permission from [67]. Copyright (2013) Elsevier. **B).** Graph illustrating the
 673 chrysotile@ZnO nanocomposites' formation process. **C)** SEM images of
 674 chrysotile@ZnO nanocomposites. **D)** Diagrammatic representation of MB's
 675 photocatalytic degradation process over chrysotile@ZnO nanocomposites in the
 676 presence of UV light. Reproduced with permission from [45], Copyright (2020)
 677 Elsevier.

678

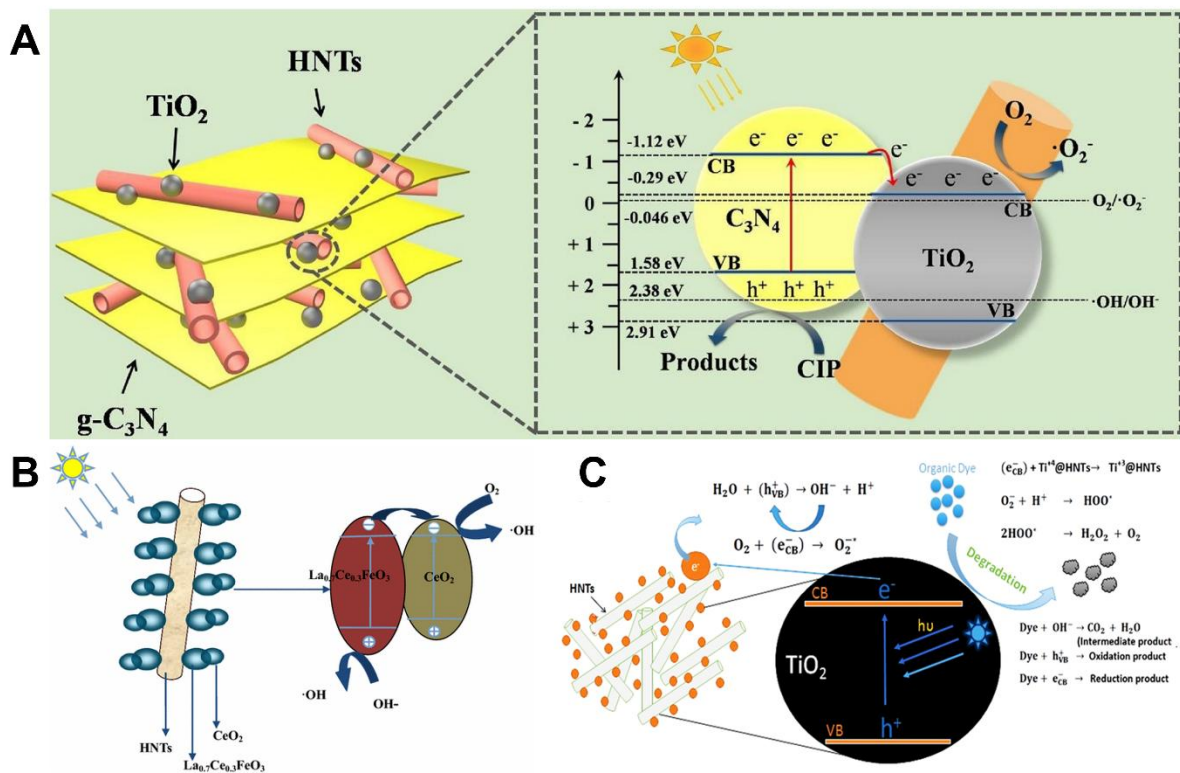
679 In a captivating study conducted by Wu and his colleagues [194], they
 680 explored the potential of novel hetero-structural g-C₃N₄/TiO₂/commercial halloysite
 681 composites in the elimination of ciprofloxacin from wastewater (**Fig, 14A**). Their
 682 findings reveal that the introduction of halloysite nanotubes (HNTs) and the g-C₃N₄-
 683 TiO₂ heterojunction significantly augmented the efficiency of charge transfer and

684 separation among photogenerated electron-hole pairs. This enhancement endowed
685 the $g\text{-C}_3\text{N}_4/\text{TiO}_2/\text{HNTs}$ hybrid material with remarkable photoelectric performance
686 and stability. Notably, the composite achieved an impressive 87% degradation of
687 ciprofloxacin within 60 minutes, owing its rapid photoelectron-hole pair transfer and
688 separation capabilities. The most significant result was the remarkable reusability of
689 the $\text{C}_3\text{N}_4/\text{TiO}_2/\text{HNTs}$ nanocomposites even after 4 cycles.

690 In a related investigation, Li et al. [195] investigated the photocatalytic
691 degradation of chlortetracycline, a common antibiotic, under visible light irradiation.
692 They achieved this by immobilizing LaFeO_3 , one of the most important perovskite-
693 type semiconductor, onto the surface of halloysite nanotubes (HNTs) through a
694 simple sol-gel method (**Fig, 14B**). Their findings indicated that untreated halloysite
695 lacked photocatalytic activity. However, when chlortetracycline was exposed to pure
696 LaFeO_3 , 74% of the drug degraded within a 90 min. Notably, the degradation rate
697 increased to 87% with the use of $\text{LaFeO}_3/\text{HNTs}$ as catalyst, underscoring the
698 enhanced performance facilitated by this composite. The improved efficacy was
699 attributed to the adsorptive capacity of HNTs and the augmented electron transfer
700 capacity of LaFeO_3 , providing insights into the synergistic mechanisms underlying
701 the composite's photocatalytic behavior.

702 In the other study, Mishra et al [99]. developed a $\text{TiO}_2@\text{HNT}$ photocatalyst
703 through a combination of sol-gel and phase inversion methods, yielding a stable and
704 highly efficient photocatalyst (**Fig, 14C**). This composite exhibited enhanced
705 photocatalytic activity attributed to the electrostatic interaction between TiO_2 and the
706 HNT surface. Under UV light, the nanocomposite effectively degraded 87.47% and
707 96.87% of methylene blue and rhodamine B, respectively. The strong electrostatic
708 interaction between TiO_2 and HNTs facilitated the generation of more electron-hole

709 pairs, thereby increasing photocatalytic activity. Particularly for methylene blue and
 710 rhodamine B dyes, which carry positive charges, HNTs improved the stability and
 711 supply of photo-generated charges, enhancing dye molecule absorption on the
 712 photocatalyst. This effect stemmed from electrostatic attractive and repulsive forces
 713 originating from the negatively charged HNTs surface. Crucially, the TiO₂@HNTs
 714 photocatalyst demonstrated non-photo-corrosive behavior during three consecutive
 715 cycles of photocatalytic degradation, highlighting its suitability for practical
 716 applications.



717

718 **Fig. 14. A)** Schematic of possible mechanism for photodegradation of CIP
 719 over g-C₃N₄/TiO₂/HNTs heterojunction composites. Reproduced with permission
 720 from [194]. Copyright (2018) Elsevier. **B).** Schematic illustration of photocatalysis
 721 mechanism for La_{0.7}Ce_{0.3}FeO₃/HNTs. Reproduced with permission from [195].
 722 Copyright (2016) Springer. **C).** Schematic representation of the photocatalytic activity
 723 of TiO₂@HNTs photocatalyst. Reproduced with permission from [99]. Copyright
 724 (2019) Springer.

725

726 Jatav et al. [196] recently conducted a hydrothermal growth of In_2S_3 on
727 aluminogermanate double-walled imogolite nanotubes. Their investigation involved
728 using methyl orange (MO) as the target pollutant for assessing photocatalytic
729 performance. The findings demonstrated that the presence of INT facilitated the
730 growth of In_2S_3 on its surface, while the morphology of In_2S_3 was significantly
731 affected by the reaction time. When the reaction time extended to three and five
732 hours, the tubular morphology of INT transformed into elongated sheets.
733 Remarkably, the photocatalytic study revealed that the In_2S_3 -decorated INT showed
734 an improvement in the rate of MO photocatalytic degradation of about 400% when
735 compared to pristine In_2S_3 , despite the composite showing a 14% increase in
736 bandgap. This improvement in photocatalytic performance was ascribed to the
737 exceptional mobility of photogenerated holes, which sped up MO's oxidative
738 processes directly.

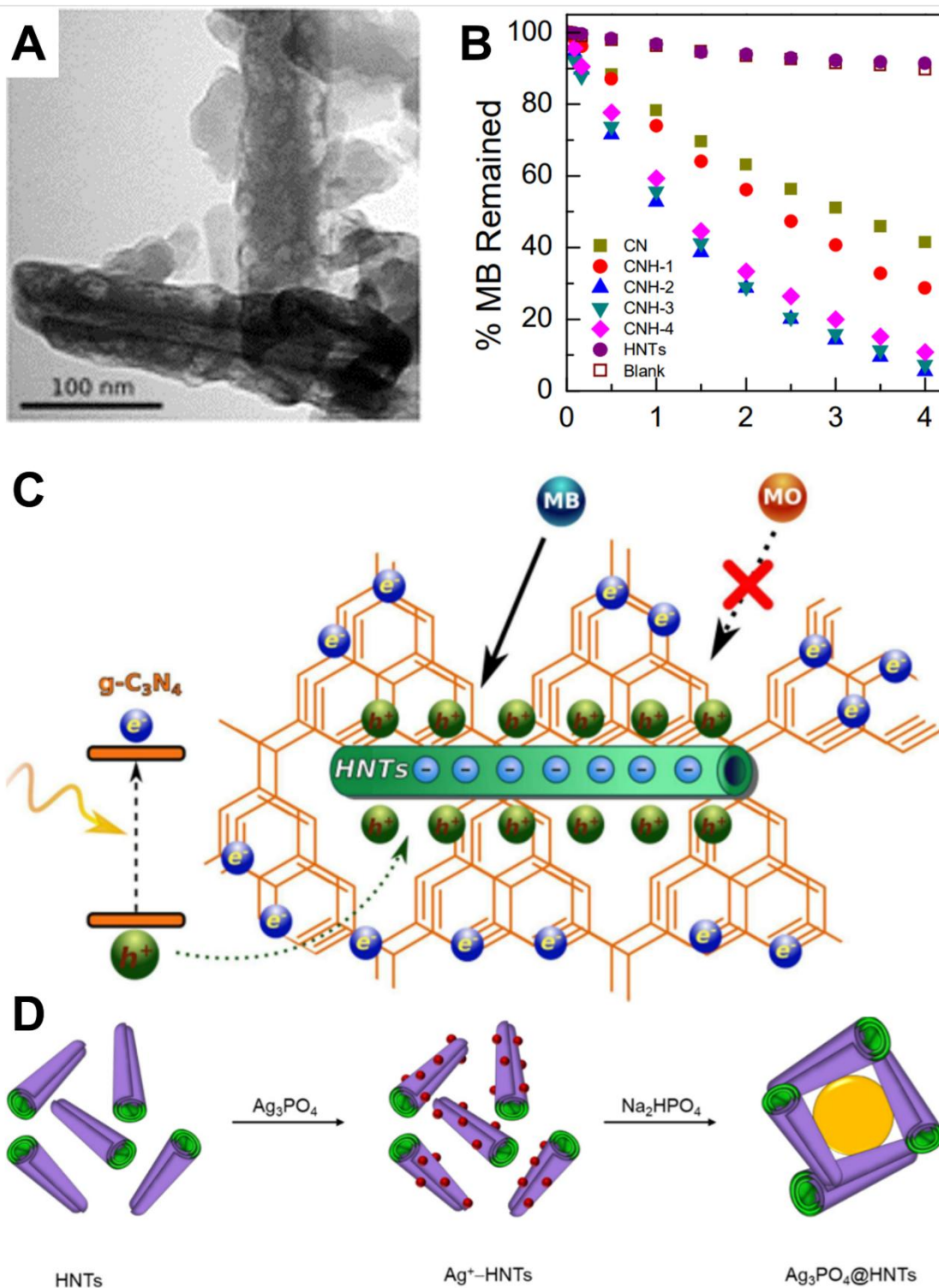
739 A literature survey reveals that using tubular clay minerals increases the
740 photocatalytic activity of several photocatalyst materials [47,197–200]. Among these
741 tubular clay materials, Halloysite stands out as one of the most widely used for
742 photocatalytic applications. Due to its tubular structure and large specific surface
743 area, it is used as a stabilizer to inhibit nanoparticle aggregation. Christoforidis et al.
744 [200] exploited the self-assembly method to generate a hetero-architecture of
745 Halloysite-graphitic carbon nitride (gC_3N_4) with different mass ratios 2, 4, 6, and 10
746 wt.% of Halloysite (denoted by CNH-x). Utilizing both pure visible light and solar light
747 simulation, the composites were then tested for the photodegradation of neutral,
748 positively, and negatively charged pollutants, including methyl orange (MO), phenol,
749 and MB. TEM images (**Fig, 15A**) proved that the deposition of small-sized gC_3N_4
750 sheets onto the halloysite surface showed no apparent aggregation. It has been

751 experimentally provided that various compositions of Hall@gC₃N₄ composites
752 exhibited photocatalytic activities greater than bare Halloysite and gC₃N₄. The best
753 composite, CNH-2 catalyst (the one containing 4 wt% of HNTs), was able to degrade
754 MB dye within 4h under solar light (**Fig, 15B**). Moreover, after four cycles of MB
755 degradation under solar-like light irradiation, the CNH-2 composite displayed no
756 noticeable decline in photocatalytic activity, signifying its remarkable photostability.
757 Moreover, adding HNTs into gC₃N₄ led to an improvement in photocatalytic activity
758 compared to gC₃N₄ alone for the degradation of neutral and positively charged
759 pollutants. This enhancement was attributed to the electrostatic interaction between
760 the negatively charged Halloysite surface and the photogenerated e⁻/h⁺ in gC₃N₄,
761 which reduced charge carrier recombination rate (**Fig, 15C**). The negatively charged
762 surface of Hal served two purposes in the case of the positively charged pollutant,
763 such as MB: it enhanced MB adsorption and moved it close to graphitic carbon
764 nitride. Conversely, the photocatalytic degradation of the negatively charged
765 substrate, like MO, was similar to that of g-C₃N₄. In this case, while the repulsion
766 between the negatively charged Halloysite and the negatively charged substrate
767 (MO) had an adverse impact, it actually led to improved charge separation,
768 consequently boosting the overall activity. Overall, Halloysite nanotubes (HNTs) had
769 demonstrated to have a double function: (a) improving the abundance and stability of
770 the photogenerated charges; (b) enhancing the adsorption of MB dye on the
771 nanocomposite. These two functions are induced by electrostatic forces, combining
772 attraction and repulsion, stemming from the negatively charged surface of HNTs.

773 Likewise, the negatively charged halloysite nanotube surface combined with
774 the electrostatic interactions of Ag cations served as a starting point to synthesize a
775 core-shell structured photocatalyst based on halloysite [199]. Subsequently, the

776 nucleation and growth of Ag_3PO_4 led to the formation of Ag_3PO_4 @halloysite
777 nanotubes (Ag_3PO_4 @HNTs) nanocomposite (**Fig, 15D**). The nanocomposites
778 exhibited remarkable photocatalytic effectiveness in decomposing RhB dye under
779 ultraviolet illumination. The outstanding photocatalytic capabilities of these
780 photocatalysts were attributed to both halloysite and Ag_3PO_4 ; mainly, halloysite
781 shells' presence guarantees rapid dye adsorption onto the catalyst surface and
782 concurrently reduces the band gap of Ag_3PO_4 , as well as minimizing the
783 recombination rate. The decrease in recombination was attributed to the lowered
784 interface defect density and the field-effect passivation produced by the negative
785 fixed charge within the halloysite shell.

786 Many works have been conducted on the photocatalytic activities of clays
787 nanotube photocatalysts to remove different types of organic pollutants, as
788 summarised in Table 1.



789

HNTs

$\text{Ag}^+\text{-HNTs}$

$\text{Ag}_3\text{PO}_4\text{@HNTs}$

790 **Fig. 15. A)** TEM images of Halloysite nanotubes@ $\text{g-C}_3\text{N}_4$, **B)** Photocatalytic
 791 degradation of MB dye over Halloysite nanotubes@ $\text{g-C}_3\text{N}_4$ under solar light
 792 irradiation. **C)** Proposed mechanism of the enhanced charge carries separation in
 793 the Halloysite nanotubes@ $\text{g-C}_3\text{N}_4$ nanocomposites. Reproduced with permission
 794 from [200], Copyright (2016) Royal Society of Chemistry. **D)** Schematic Illustration of
 795 core-shell structured $\text{Ag}_3\text{PO}_4\text{@Hal}$ nanocomposites formation process $\text{Ag}_3\text{PO}_4\text{@Hal}$
 796 nanocomposites. Reproduced with permission from [199], Copyright (2017) Elsevier.

797

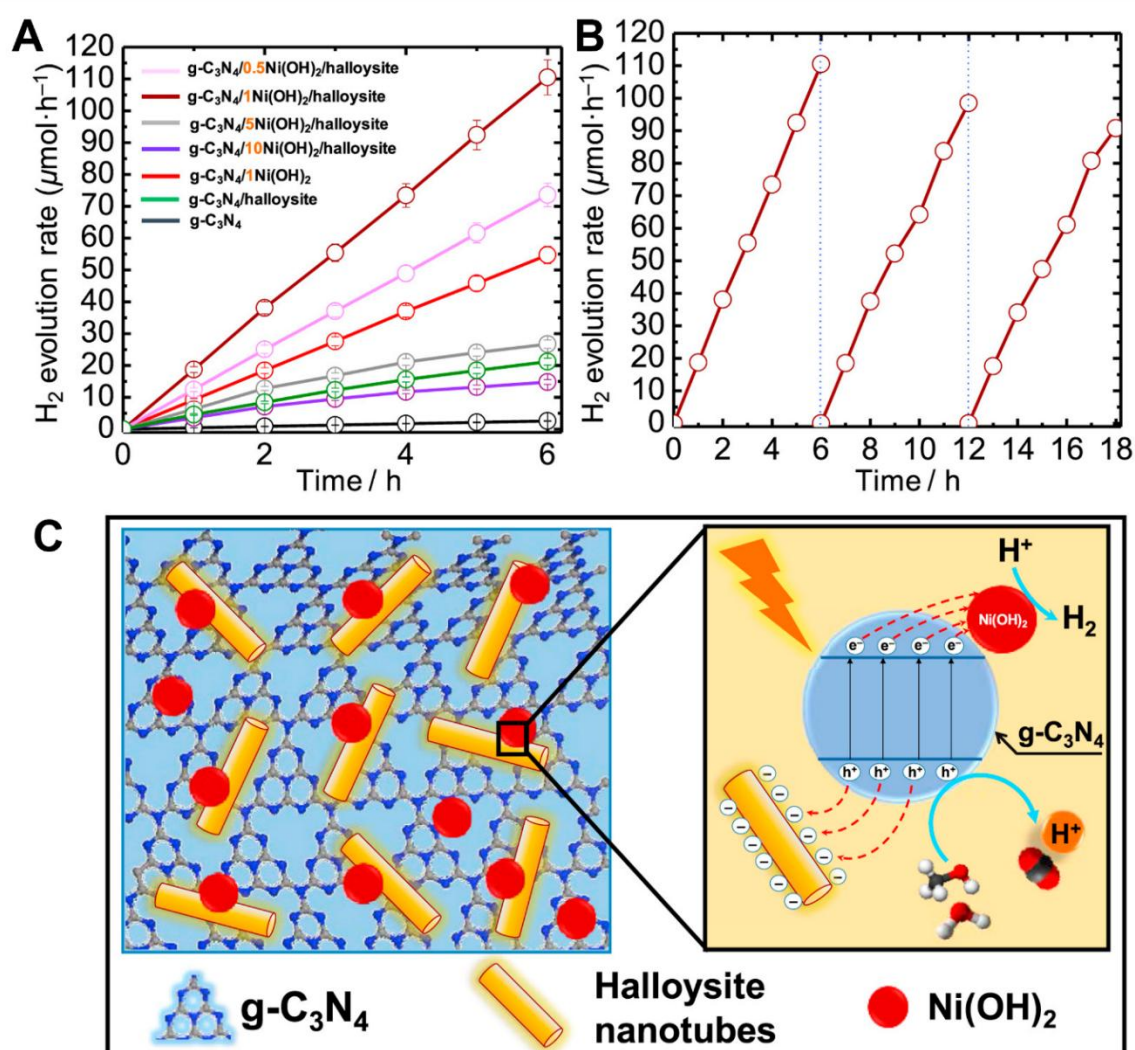
Table. 1. Studies of clay nanotubes photocatalysts for various pollutants

Clay nanotube	Photocatalyst	light source	Pollutants	Photocatalytic degradation activity	Ref
Chrysotile	Chrysotile@SnO ₂	Hg lamp (centered at 450 nm, 250 W)	MB dye	99% (90 min)	[47]
	Chrysotile@ZnO	250 W high-voltage Hg lamp (365 nm)	MB dye	99.5% (60 min)	[45]
	Chrysotile@ZnO	365 nm UV light	4-nitrophenol	39% (300 min)	[98]
	Chrysotile@TiO ₂	Xe light source	CV dye	~66% (240 min)	[201]
Imogolite	Fe-0.050-MeIMO	8 W mercury vapor lamp emitting at 254 nm	TRZ dye	100% (300min)	[202]
	Me-IMO	8 W mercury vapor lamp emitting at 254 nm	TRZ dye	80% (300min)	[202]
	INT-In ₂ S ₃	300 W Xe lamp	MO dye	90% (120min)	[196]
	TiO ₂ -IMO	UV light lamp (1.0 mW/cm ²)	CH ₃ CH ₂	90% (60min)	[67]
Halloysite	Halloysite@Fe ₂ O ₃	UV low pressure Hg immersion lamp TNN 15/32	2,6-dichloroaniline (26DCA)	84.6% (300 min)	[203]
	Halloysite@TiO ₂	UV low pressure Hg immersion lamp TNN 15/32	2-chloroaniline (2CA)	84.9% (300 min)	[203]
	Ag ₃ PO ₄ -25 wt% HNTs	26 W Sylvania visible lamp.	naproxen sodium	~80% (10 min)	[204]
	La ₂ O ₃ /CeVO ₄ @halloysite	300 W Xenon lamp ($\lambda \geq 420$ nm)	TC dye	87.1% (60 min)	[205]
	N-TiO ₂ / Halloysite	xenon lamp, PLS-SXE300, 300W	phenol	70% (150 min)	[206]
	Ag ₂ CO ₃ -75 wt.% Halloysite	26 W Sylvania visible lamp	RhB dye	97 % (40 min)	[207]
	CdS@Halloysite	xenon lamp, 500W	TC dye	93% (60 min)	[208]
	Ag@ Halloysite	500 W mercury lamp	TC dye	95.81% (80 min)	[209]
	Ag/AgBr/ Halloysite	200 W xenon lamp with a UV cutoff filter	RhB dye	98%% (30 min)	[210]
	AgNPs@N-Halloysite	500 W xenon lamp	MB dye	90% (60 min)	[211]
	Co ₃ O ₄ @ Halloysite	60 W high-pressure mercury lamp	MB dye	97 % (120 min)	[197]
	Halloysite@W18O ₄₉	300 W Mercury lamp	MO dye	99 % (120 min)	[198]
	Bi ³⁺ - CdS/Halloysite	500 W xenon lamp	TC dye	90% (30 min)	[212]
	Ce-TiO ₂ /HNT	300 W Xe lamp ($\lambda > 420$)	Tetracycline	78% (60 min)	[213]
	Carbon-TiO ₂ -HNT (8%)	50 W UV lamps ($\lambda < 420$ nm)	MB dye	81% (90 min)	[214]
	Pani-TiO ₂ -HNT (0.5 g/L)	XPA-7 photochemical system (800 W Xe lamp)	RhB dye	76.49 % (360 min)	[215]
Amylose-HNT-TiO ₂	12 W UV lamp ($\lambda = 253$ nm)	4-nitrophenol	90% (240 min)	[216]	

801 **4.2. Photocatalytic water splitting**

802 Photocatalytic water splitting has been widely explored as a vital clean energy
803 source. Photogenerated electrons and holes are simultaneously generated when
804 exposed to light in the general mechanism of photocatalytic water splitting for
805 hydrogen production. Following this, electrons and holes migrate to the
806 photocatalyst's surface to participate in the reaction. The photocatalyst's potential
807 and valence band level should be positioned at a lower energy level than H^+/H_2 and
808 higher than OH^-/O_2 potential [9,15,217]. To ensure a successful H_2 evolution
809 reaction, the photocatalyst's conduction band (CB) energy level must be below 0 V
810 versus the normal hydrogen electrode (NHE) at pH 7. Similarly, for effective H_2O
811 oxidation, the valence band (VB) energy level should be above 1.23 V versus NHE.
812 Therefore, theoretically, for water splitting, the lowest bandgap is 1.23 eV. These
813 energy level requirements are vital to promote favorable redox processes during
814 photocatalysis. Recently, it was proven that using clay nanotubes could improve
815 photocatalytic activity and facilitate separation and recycling [205,208].
816 Hojamberdiev and co-workers [218] stated that the synthesis of a novel $Ni(OH)_2@g-$
817 C_3N_4 /halloysite composite photocatalyst by mixing an easily prepared gC_3N_4 with
818 low-cost $Ni(OH)_2$ nanoplatelets, inexpensive and earth-abundant halloysite
819 nanotubes. The obtained composite was used as an efficient photocatalyst for
820 hydrogen evolution. As-prepared photocatalysts' hydrogen evolution reaction activity
821 was assessed using an aqueous solution with 10 vol% methanol as a sacrificial
822 agent. The investigation of the $Ni(OH)_2$ loading effect showed that the 1 wt%
823 $Ni(OH)_2@g-C_3N_4$ /halloysite photocatalyst exhibited the maximum photocatalytic
824 hydrogen evolution rate ($18.42 \mu\text{mol}\cdot\text{h}^{-1}$) compared to $Ni(OH)_2@g-C_3N_4$ (9.12
825 $\mu\text{mol}\cdot\text{h}^{-1}$) and was 40 times higher than $g-C_3N_4$ alone ($0.43 \mu\text{mol}\cdot\text{h}^{-1}$) (**Fig. 16A**).
826 Furthermore, 1 wt% $Ni(OH)_2@g-C_3N_4$ /halloysite photocatalyst showed negligible

827 decrease in H_2 evolution activity after three cycles (**Fig. 16B**). The halloysite's
 828 negatively charged surface, which effectively traps photogenerated holes, lowers the
 829 rate of electron-hole recombination, and lengthens the electron lifespan, provided an
 830 explanation for these results (**Fig. 16C**). Moreover, a computational model was
 831 employed to assess the adsorption properties of H_2O and $MeOH$ molecules on the
 832 catalyst surface. The findings indicated that the presence of halloysite, $g-C_3N_4$ and
 833 $Ni(OH)_2$ enhanced the adsorption of water and methanol on the co-catalyst surface.



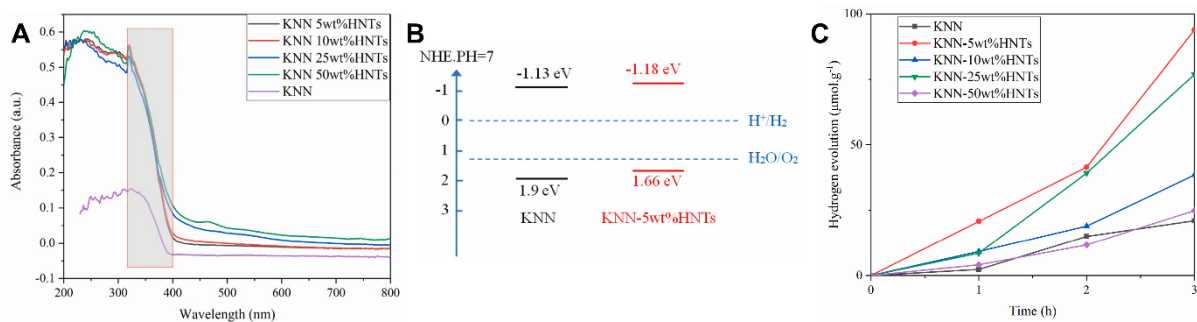
834

835 **Fig. 16. A)** $Ni(OH)_2@g-C_3N_4/halloysite$ nanocomposites: reaction time courses of
 836 visible light-driven hydrogen evolution. **B)** Reaction time courses of visible-light-
 837 driven hydrogen evolution on $1.0Ni(OH)_2@g-C_3N_4/halloysite$ nanocomposite for three
 838 successive runs. **C)** Graphical representation of the evolution of photocatalytic
 839 hydrogen evolution over developed nanocomposites, showing the separation and

840 transfer of photogenerated charge carriers. Reproduced with permission from [218],
841 Copyright (2019) Elsevier.

842

843 Recently, Lu et al. [219] successfully synthesized several
844 $K_{0.5}Na_{0.5}NbO_3$ /halloysite nanocomposites by changing the halloysite concentration
845 from 0 to 25 wt.% via a solid phase reaction process. These hybrid samples were
846 then used to analyze the photocatalytic hydrogen evolution performance under UV
847 light illumination (Xenon arc lamp). The authors demonstrated that by incorporating
848 halloysite (HNTs), the absorption spectrum of $K_{0.5}Na_{0.5}NbO_3$ (KNN) exhibited a
849 substantial enhancement in the UV region, with the absorption intensity in the 200-
850 300 nm range increasing approximately two-fold (**Fig. 17A**). Introducing HNTs into
851 KNN reduced the band gaps from 3.03 eV to 2.64 eV (**Fig. 17B**). Moreover, the
852 authors demonstrated that the conduction band (E_{CB}) of KNN-5wt%HNTs
853 nanocomposite was changed to a lesser value from -1.13 eV to -1.18 eV compared
854 with the pure $K_{0.5}Na_{0.5}NbO_3$, providing more straightforward water reduction to
855 hydrogen. Notably, the composite material KNN-5wt%HNTs demonstrated an
856 excellent hydrogen production performance ($31.28 \mu\text{mol}\cdot\text{g}^{-1} \text{h}^{-1}$) under UV light
857 irradiation, producing 4.48 times as much H_2 as $K_{0.5}Na_{0.5}NbO_3$. (**Fig. 17C**). The
858 findings of this study confirm that the judicious incorporation of halloysite can
859 improve H_2 production efficiency.



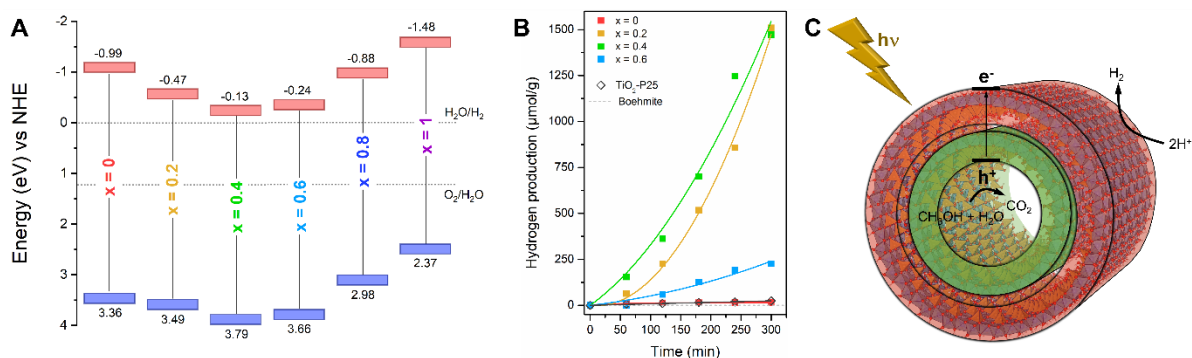
860

861 **Fig. 17.** $K_{0.5}Na_{0.5}NbO_3$ -halloysite nanotubes composites. **A)** Spectra of optical
862 absorption, **B)** illustrative sketch of the energy band structures and **C)** hydrogen

863 evolution reaction for different composites. Reproduced with permission from [219],
864 Copyright (2022) Elsevier.

865

866 In a recent research conducted by our research group [220], we achieved a
867 milestone in literature by modifying double-walled aluminogermanate INTs through
868 the incorporation of titanium into the NT walls. The precursor ratio, denoted as $x =$
869 $[Ti]/([Ge]+[Ti])$, was varied between 0 and 1. The optical properties of the catalysts
870 we prepared revealed a significant reduction in the band gap (E_g) energy from 4.35
871 eV (for pristine Ge-DWINT) to 3.96 eV ($x = 0.2$) and further to 3.92 eV ($x = 0.4$).
872 Increasing the Ti/Ge ratio consistently decreased the E_g to 3.85 eV. Additionally, Ti-
873 doping initially caused a downward shift of the VB edge (0.13 and 0.43 eV for ratios
874 of 0.2 and 0.4, respectively), followed by an upward shift with further increases in the
875 Ti/Ge ratio. A similar trend was observed for the CB edge, which shifted down to -
876 0.13 eV (for a ratio of 0.4) and up to -1.43 eV (**Fig. 18A**). Interestingly, this evolution,
877 with an optimum around $x = 0.4$, coincided with the disappearance of nanotubes in
878 favor of boehmite and anatase phases. We examined the photocatalytic properties of
879 the prepared photocatalysts for H_2 production under artificial solar-light irradiation to
880 assess the impact of Ti-doping. Optimal ratios were determined at $x = 0.2$ and $x =$
881 0.4, yielding H_2 production rates of 1509 and 1472 $\mu\text{mol g}^{-1}$, respectively (**Fig. 18B**).
882 These rates surpassed those of the composites, bare reference, and TiO_2 P25
883 benchmark NP SC. The enhanced photoactivity stemmed from the narrowed band
884 gap and downward shifts of the CB edges in both composites. As illustrated in **Fig.**
885 **18C**, photogenerated charges (e^-/h^+) trigger dissociative adsorption of sacrificial
886 electron donors (SED) and hole scavenging, leading to the release of hydrogen ions
887 (H^+) within the nanotube's internal cavity. Reduction, resulting in H_2 formation,
888 predominantly occurs on the outer surface of the nanotubes, while oxidation
889 predominantly occurs within the nanotubes.



890

891 **Fig. 18. A)** energy diagram scheme of the Ti/Ge samples as a function of the
 892 substitution ratio. **B)** Hydrogen evolution reaction under solar-light irradiation for a)
 893 Ge-DWINT and Ti/Ge samples with different ratios. **C)** Schematic illustration of the
 894 proposed H₂ production mechanism. Reproduced with permission from [220],
 895 Copyright (2023) wiley.

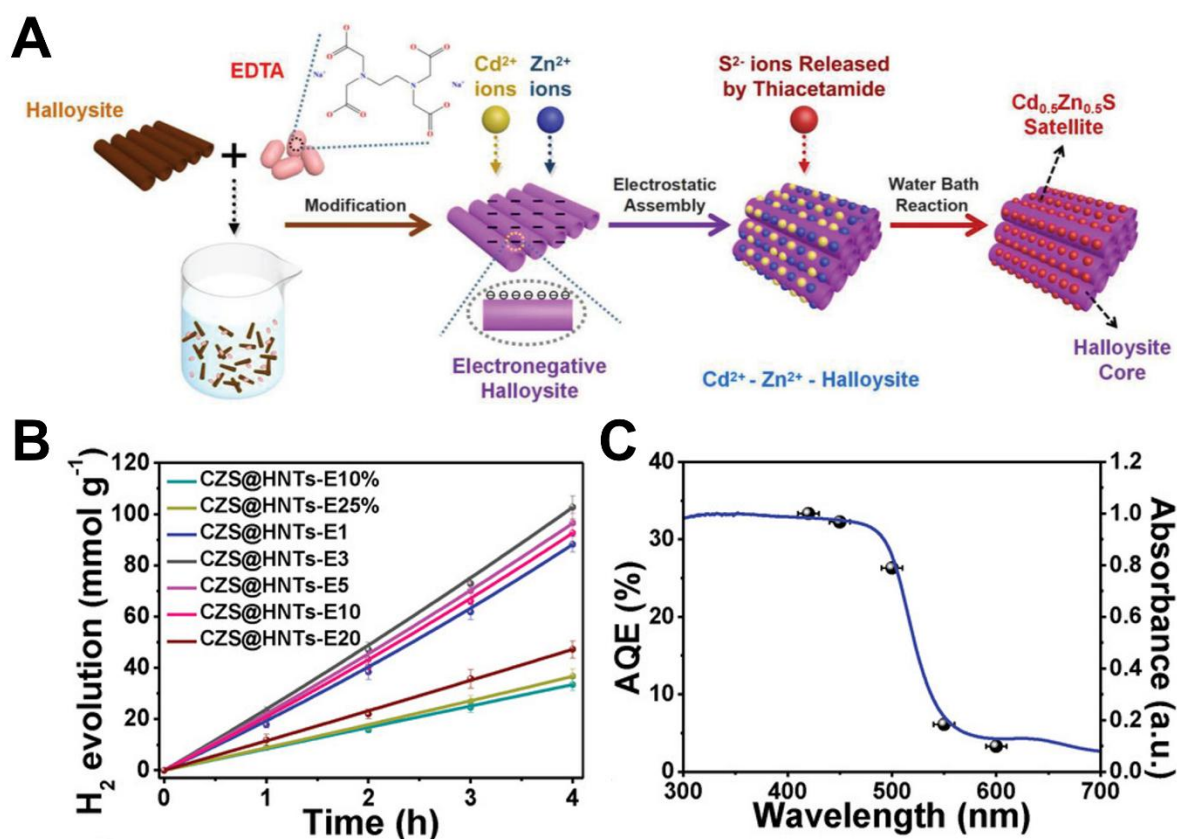
896

897 In an intriguing study conducted by Zhang et al. [221], they fabricated a
 898 satellite-core structured Cd_{0.5}Zn_{0.5}S@halloysite hollow nanotubes with a 0D-1D
 899 configuration, modified by EDTA with varying amounts, denoted as CZS@HNTs-EX.
 900 This was achieved through a facile in-situ assembly approach for photocatalytic H₂
 901 evolution. As depicted in **Fig. 19A**, the organic solvent EDTA was initially employed
 902 to modify the halloysite, rendering its surface negatively charged. Then, because of
 903 the electrostatic attraction Cd²⁺ and Zn²⁺ cations were added and adsorbed onto the
 904 halloysite. The addition of thioacetamide finally caused the Cd_{0.5}Zn_{0.5}S nanospheres
 905 to grow in situ on the surface of the halloysite that had been modified by EDTA. It
 906 was highlighted in this work that the CZS@HNTs-E3% composite exhibited an
 907 appealing photocatalytic H₂ evolution after 4 hours of illumination with a yield of
 908 102.67 mmol g⁻¹ (**Fig. 19B**) and high apparent quantum efficiency (AQE) of 32.29%
 909 at λ = 420 nm, higher than majorities of H₂ evolution photocatalysts (**Fig. 19C**). Only
 910 a slight decrease in H₂ production was observed after five cycles, while maintaining
 911 the crystallinity and morphology of the CZS@HNTs-E3% hollow nanotubes. This
 912 highlights the potential of recyclable catalysts for industrial applications.

913 Furthermore, the authors demonstrated that the enhancement of the photocatalytic
914 of CZS@HNTs-EX was attributed to the succeeding factors: I) the hollow
915 architecture of halloysites caused by several reflections and scattering of light within
916 the cavity, extending the optical transmission path and enhancing the light utilization.
917 II) Halloysites allow an excellent dispersion of $\text{Cd}_{0.5}\text{Zn}_{0.5}\text{S}$, promoting the diffusion of
918 charge carriers to the catalyst-solution interface. III) EDTA embedded on halloysites
919 draws and uses considerable photogenerated h^+ , promoting the charge separation of
920 e^- and h^+ , permitting more e^- to migrate to the surface of $\text{Cd}_{0.5}\text{Zn}_{0.5}\text{S}$ for participation
921 in the reductive reaction. IV) Owing to the h^+ capture, the h^+ -dominated photo-
922 oxidation of S^{2-} in $\text{Cd}_{0.5}\text{Zn}_{0.5}\text{S}$ is hindered, causing excellent photochemical stability
923 in CZS@HNTs-E3.

924 As far as we are aware, no research has been conducted on the utilization of
925 imogolite or chrysotile for photocatalytic water splitting. It is, therefore, important to
926 pursue efforts in this direction. Given the success of halloysite-based composites in
927 promoting photocatalytic hydrogen evolution, it is reasonable to believe that
928 imogolite and chrysotile might exhibit similar or superior effects.

929



930

931 **Fig. 19.** **A)** Schematic representation of the EDTA-mediated CZS@HNT synthesis
 932 process. **B)** Hydrogen evolution time courses for CZS@HNTs-EX samples with
 933 varying EDTA to halloysite mass ratios. **C)** Photocatalytic performance of
 934 CZS@HNTs-E3 under monochromatic light irradiation: UV-vis spectrum and
 935 wavelength dependence. Reproduced with permission from [221], Copyright (2019)
 936 WILEY.

937

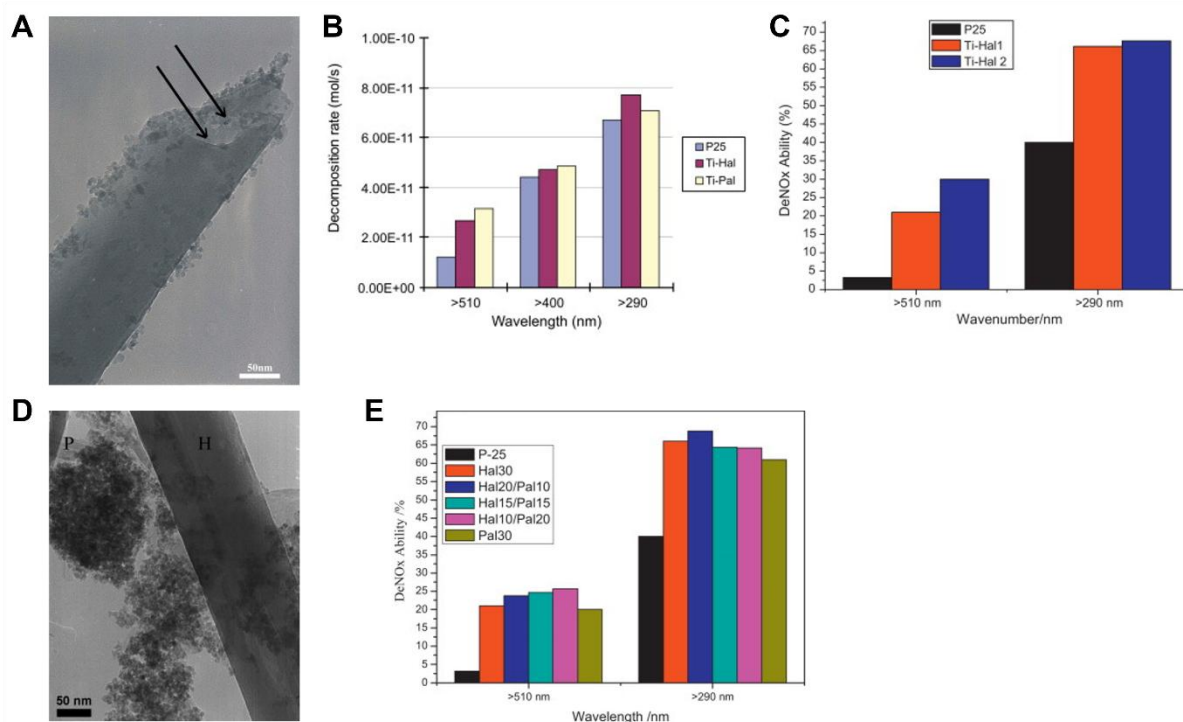
938 4.3. Photocatalytic removal of NO_x

939 Nitric oxide (NO_x) emission into the atmosphere is causing increasing concern.
 940 This pollutant is produced through fossil fuel utilization and combustion of industrial
 941 burners. The NO_x emitted into the atmosphere causes acid rain [221–224], climate
 942 changes, and ozone layer destruction [222,223]. Thus, its quantitative removal or
 943 reduction is highly desired. In fact, numerous catalytic processes for the conversion
 944 of nitrogen gases (e.g., NO and NO₂) into oxygen (O₂), nitrogen (N₂), or nitrate (NO₃⁻
 945) have been developed, including adsorption, selective catalytic reduction,
 946 nonselective catalytic reduction, wet scrubbing, and biofiltration. However, these

947 techniques can only be used to treat NO_x in extreme concentrations; their efficiency
948 and economic benefits are reduced at lower NO_x concentrations. Currently, for low-
949 concentration NO_x in the air at room temperature, the photocatalytic removal of NO_x
950 is regarded as a green and low-cost technology and has attracted much attention.
951 Indeed, some studies have removed or reduced the NO_x through clay nanotube
952 systems. For instance, to remove NO_x in the presence of UV and Visible light
953 irradiation, Papoulis et al. [224] reported a sol-gel approach for forming
954 TiO₂@halloysite nanocomposites. This was performed under hydrothermal
955 conditions with a halloysite sample from Limnos Island in Greece. The TEM results
956 of the as-prepared nanocomposite exhibited an excellent distribution of TiO₂ on the
957 external surfaces of the halloysite nanotube (**Fig. 20A**). The halloysite acts as a clay
958 stabilizer, preventing the aggregation of nanoparticles because of its substantial
959 specific surface area and its tubular surface [197,198]. The photocatalytic results
960 clearly show that the as-prepared TiO₂@halloysite nanocomposite has significantly
961 better photocatalytic efficiency in decomposing NO_x gas when exposed to UV ($\lambda =$
962 290 nm) and visible light ($\lambda = 510$ nm) illumination: these are, respectively, 2.61 and
963 1.15 times higher than pristine commercial TiO₂ (P25), (**Fig. 20B**). The well-
964 dispersed TiO₂ has explained this higher activity on the halloysite surface. The same
965 research group used the same method to synthesize two TiO₂@halloysite
966 nanocomposites, utilizing halloysite from two distinct geographical regions: Greece
967 and the USA [68]. The two clays showed a good dispersion of TiO₂ NPs in their
968 respective nanocomposites, and both had interparticle mesopores measuring
969 approximately 5.7 nm. It was observed that both nanocomposites demonstrated
970 promising photocatalytic performance for the NO_x gas decomposition under visible
971 light ($\lambda = 510$ nm) and UV light irradiation ($\lambda = 290$ nm) (**Fig. 20C**). The

972 TiO₂@halloysite nanocomposite with halloysite from the USA demonstrated higher
973 photocatalytic performance, likely due to its larger specific surface area. (187 m²/g).

974 Furthermore, it also revealed considerably improved photocatalytic activity for
975 NO_x gas decomposition under visible light ($\lambda = 510$ nm) and UV light irradiation ($\lambda =$
976 290 nm), which are, respectively, 9.38 and 1.69 times higher than pristine
977 commercial TiO₂ (P25) (**Fig. 20C**). In another study by the same research group
978 [225], a three-phase nanocomposite was prepared using two distinct nanoclay
979 minerals, halloysite, and palygorskite, in combination with TiO₂ (denoted by Hal:
980 PAL-TiO₂) (**Fig. 20D**). The authors demonstrated that the Hal:PAL-TiO₂
981 nanocomposite exhibited a grey color with enhanced absorption in the visible light
982 region compared to titania P25, which showed no absorption in the same region. The
983 photocatalytic activity of these systems was further evaluated in this system by
984 decomposing the NO_x gas as a function of irradiation time. The results
985 demonstrated that the Hal:PAL-TiO₂ nanocomposite displayed significantly higher
986 activity than the commercial TiO₂ P25 under both UV and visible light irradiation, with
987 up to 8 times higher efficiency under UV light and 1.72 times higher efficiency under
988 visible light (**Fig. 20E**).



989

990 **Fig. 20. A)** TEM images showing TiO₂ grains of about 3–15 nm on halloysite tubes
 991 **B)** Photocatalytic activities in decomposing NO_x gas by commercial titania P25,
 992 TiO₂-treated halloysite (Ti-Hal) and TiO₂-treated palygorskite. Reproduced with
 993 permission from [224], Copyright (2010) Elsevier. **C)** Photocatalytic activities in
 994 decomposing NO_x gas by commercial titania P25, TiO₂-treated halloysite (from
 995 Greece) and TiO₂-treated halloysite (from USA). Reproduced with permission from
 996 [68], Copyright (2013) Elsevier. **D)** TEM micrographs showing the three-phase
 997 nanocomposites Hal10:Pal20-TiO₂. **E)** Photocatalytic activity for NO_x gas
 998 decomposition by commercial titania (P25), single clay-TiO₂, and three-phase
 999 nanocomposites. Reproduced with permission from [225], Copyright (2014) Elsevier.

1000

1001 4.4. Photocatalytic disinfection of bacteria

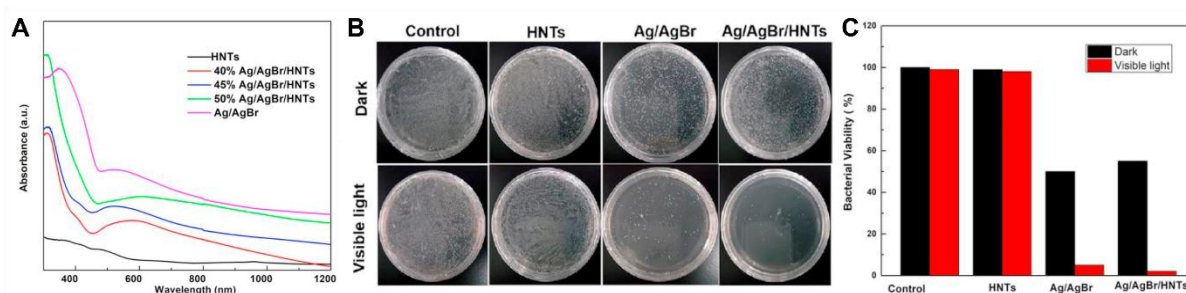
1002 Disinfection of bacteria is of particular importance. Numerous efforts have been
 1003 dedicated to developing environmentally friendly technologies for disinfecting
 1004 microorganisms in water [226–228]. However, despite traditional water disinfection
 1005 technologies such as ozone, chlorination, and ultraviolet methods, they have many
 1006 disadvantages. For example, they may be chemically or energy-demanding and
 1007 produce toxic by-products. Photocatalytic disinfection of bacteria, on the other hand,
 1008 is a non-toxic and eco-friendly process that does not create any harmful by-products.

1009 Escherichia coli is a reliable indicator of water quality concerns within the diverse
1010 spectrum of bacteria, often signaling potential fecal contamination due to its
1011 presence [226]. The performance of nanotube clay photocatalysts in such
1012 applications has been recently investigated. For instance, Xu et al. [210] successfully
1013 synthesized a novel composite consisting of Ag/AgBr/halloysite nanotube via a facile
1014 sol-gel method and used it to kill gram-negative bacterium *E. Coli* when exposed to
1015 visible light. This study's findings revealed that all Ag/AgBr/halloysite
1016 nanocomposites exhibited strong absorption in the range of 300 to 1000 nm (**Fig.**
1017 **21A**). Furthermore, according to the PL spectrum, the Ag/AgBr/halloysite nanotube
1018 emitted relatively weak light compared to Ag/AgBr alone, signifying higher separation
1019 of the photoexcited electron-hole pairs in the composites and indicating enhanced
1020 photocatalytic activity. According to the findings of this study, it was found that when
1021 the bacteria was treated with 45% Ag/AgBr/halloysite nanotube composite under
1022 irradiation, up to 98% of *E. Coli* was killed, surpassing the efficacy of Ag/AgBr alone
1023 under the same conditions (**Fig. 21B and 21C**). Based on this study's experimental
1024 observation and characterization results, the formation of the composite is the key
1025 factor behind the increased photocatalytic disinfection of bacteria.

1026 In the presence of the Ag/AgBr/halloysite nanotube composite, the photocatalytic
1027 mechanisms are as follows: first, the halloysite nanotube serves as the supporting
1028 structure in the composite, preventing the decomposition of Ag/AgBr particles; then,
1029 the charged surface of the halloysite efficiently improves the separation of electron-
1030 hole pairs and promotes the adsorption of *E. Coli*.

1031 The earlier studies show that halloysite has received considerable attention as a
1032 photocatalyst. However, it is essential to highlight that research concerning the use
1033 of imogolite or chrysotile for photocatalytic bacterial disinfection has been scarcely

1034 explored. This is not so surprising in the case of chrysotile since these nanotubes
1035 are known to be toxic, limiting their use. For imogolite nanotubes, some research
1036 groups have explored their potential for treating pathogenic bacteria without
1037 employing photocatalysis techniques [229,230]. While these investigations represent
1038 a valuable exploration of imogolite's antimicrobial properties, they also emphasize
1039 the need for additional research to unlock its full potential for combating bacterial
1040 contamination.



1041 **Fig. 21. A)** UV-Vis absorption spectra of Ag/AgBr/Halloysite nanotube
1042 nanocomposite. **B)** Photographs of colonies of *E. coli* treated with HNTs, Ag/AgBr,
1043 and 45%Ag/AgBr/HNTs without and with visible light irradiation, respectively; **C)**
1044 Histograms of *E. coli* viability. Reproduced with permission from [210], Copyright
1045 (2021) Elsevier.

1047 5. Conclusion and future perspectives

1049 Nanosized tubular clay materials have garnered significant interest due to
1050 their distinctive physicochemical characteristics. The most representative examples
1051 of tubular clay materials are imogolite, halloysite, and chrysotile. Although these
1052 clays have similar morphology, their chemical structure and properties differ.

1053 Considering that these nanotubular clay materials have a high surface area
1054 arising from their nanotubular structure, large pore volumes, higher adsorption
1055 capacity, and good mechanical properties, they could offer a wide range of promising
1056 applications in photocatalysis. Moreover, these tubular clays also serve as easily

1057 obtainable and low-cost supports to prevent the aggregation of semiconductor
1058 materials. However, the only drawback of using these materials as photocatalysts is
1059 their wide band gap, which limits their potential in photocatalytic reactions.

1060 Thus, the primary aim of this review has been to compile an extensive
1061 overview over several decades, including the recent trends in the development of
1062 imogolite, halloysite, and chrysotile, as well as their main physicochemical
1063 properties. Furthermore, we have systemically provided an overview of current
1064 research progress on these materials for photocatalytic applications, mainly focusing
1065 on their intrinsic merits and the challenging aspects of photocatalysis. This review
1066 has also elucidated their versatile photocatalytic applications, including the
1067 decomposition of organic dye contaminants, selective organic transformation via
1068 photocatalysis, hydrogen generation, bacterium disinfection, and reducing nitrogen
1069 oxide (NO_x) pollution.

1070 Although research has been done on using clay nanotubes as photocatalysts,
1071 substrates, or in combination with other photocatalysts in heterogeneous
1072 photocatalysis, most investigations in this domain remain in their early stages.
1073 Therefore, based on this review, future research should prioritize the following
1074 aspects:

1075 (i) Most current research combines imogolite, halloysite, and chrysotile with
1076 traditional semiconductors (such as TiO₂ and ZnO). Future research should
1077 attempt to combine these clays with new semiconductors. For example, it is
1078 possible to develop a co-catalyst without precious metals that can be added to
1079 these clay nanotube-based photocatalysts. In addition, the cost should be
1080 carefully considered for industrial applications.

- 1081 (ii) Although numerous studies have examined the photocatalytic capabilities of
1082 clay nanotube-based nanocomposites in degrading dye pollutants, most of
1083 these works have focused solely on MB, RhB, TC, and MO dyes. Therefore, it
1084 is imperative to extend the range of organic pollutants like antibiotics, drug
1085 components, and pesticides to assess the photocatalytic degradation potential
1086 of such materials comprehensively.
- 1087 (iii) This review also recommends using actual polluted water instead of
1088 simulated wastewater and emphasizes the importance of measuring
1089 degradation efficiency through parameters such as TOC removal
1090 percentage. Standardization of measurements is also desirable in order to
1091 compare the different systems, particularly in terms of stability.
- 1092 (iv) Undoubtedly, there is a substantial need for in-depth research to elucidate
1093 the detailed photocatalytic mechanism of clay nanotubes. This requires the
1094 utilization of innovative characterization and computational methods,
1095 including but not limited to density functional theory (DFT). Such
1096 investigations are crucial for enhancing our understanding of these materials
1097 and their photocatalytic processes. There are many more photocatalytic
1098 experiments in reducing CO₂ in the presence of imogolite, halloysite, and
1099 chrysotile that can be done. This research field seems promising and, to our
1100 knowledge, has not yet been investigated by any researcher, nor has there
1101 been any published data.
- 1102 (vi) Future experimental research will be motivated by imogolite's potential to
1103 improve polarization in photocatalytic applications, given its natural
1104 polarizability and ease of manufacture. This implies that imogolite will soon be
1105 used for energy conversion, adding a new substance to the vast field of
1106 photocatalysis.

1107 (vii) The current research on imogolite, halloysite, and chrysotile photocatalysts
1108 predominantly centers around small-scale laboratory investigations. The focus
1109 should shift towards creating environmentally friendly large-scale preparation
1110 methods in the future.

1111 Compared to similar nanotube materials, like CNTs, the current study of clay
1112 nanotube photocatalysts still needs to be improved. From the number of applications
1113 reported in our review article, we conclude that halloysite, chrysotile, and imogolite
1114 are versatile materials that can provide new opportunities and directions in the field
1115 of photocatalysis.

1116 **Acknowledgment:**

1117 This work is supported by “Investissements d’Avenir” LabEx PALM (ANR-10-LABX-
1118 0039-PALM, project SP3).

1119

1120 **References**

- 1121 [1] Saidur R, Abdelaziz EA, Demirbas A, Hossain MS, Mekhilef S. A review on
1122 biomass as a fuel for boilers. *Renew Sustain Energy Rev* 2011;15:2262–89.
1123 <https://doi.org/10.1016/j.rser.2011.02.015>.
- 1124 [2] Ajmal Z, Naciri Y, Hsini A, Bresolin BM, Qadeer A, Muhammad Nauman MA,
1125 et al. Prospects of Photocatalysis in the Management of Nitrate Contamination
1126 in Potable Water. 2021. https://doi.org/https://doi.org/10.1007/978-3-030-70757-6_7.
- 1128 [3] Bouziani A, Yahya M, Naciri Y, Hsini A, Khan MA, Sillanpää M, et al.
1129 Development of polyaniline coated titania-hematite composite with enhanced
1130 photocatalytic activity under sun-like irradiation. *Surfaces and Interfaces*
1131 2022;34:102328. <https://doi.org/10.1016/J.SURFIN.2022.102328>.
- 1132 [4] Tanji K, El Mrabet I, Fahoul Y, Jellal I, Benjelloun M, Belghiti M, et al.
1133 Epigrammatic progress on the photocatalytic properties of ZnO and TiO₂
1134 based hydroxyapatite@photocatalyst toward organic molecules
1135 photodegradation: A review. *J Water Process Eng* 2023;53:103682.
1136 <https://doi.org/10.1016/J.JWPE.2023.103682>.
- 1137 [5] Li J, Jiménez-Calvo P, Paineau E, Ghazzal MN. Metal chalcogenides based
1138 heterojunctions and novel nanostructures for photocatalytic hydrogen
1139 evolution. *Catalysts* 2020;10. <https://doi.org/10.3390/catal10010089>.
- 1140 [6] Li A, Zhu W, Li C, Wang T, Gong J. Rational design of yolk-shell
1141 nanostructures for photocatalysis. *Chem Soc Rev* 2019;48:1874–907.
1142 <https://doi.org/10.1039/c8cs00711j>.

- 1143 [7] Zhang T, Wang T, Meng F, Yang M, Kawi S. Recent advances in ZnIn₂S₄-
1144 based materials towards photocatalytic purification, solar fuel production and
1145 organic transformations. *J Mater Chem C* 2022;10:5400–24.
1146 <https://doi.org/10.1039/d2tc00432a>.
- 1147 [8] UNDP. World Energy Assessment. Energy and the challenge of Sustainability.
1148 2000. <https://doi.org/10.1109/ICEE.2017.7893438>.
- 1149 [9] Jiménez-Calvo P, Caps V, Ghazzal MN, Colbeau-Justin C, Keller V.
1150 Au/TiO₂(P25)-gC₃N₄ composites with low gC₃N₄ content enhance TiO₂
1151 sensitization for remarkable H₂ production from water under visible-light
1152 irradiation. *Nano Energy* 2020;75.
1153 <https://doi.org/10.1016/j.nanoen.2020.104888>.
- 1154 [10] Wong WY, Ho CL. Organometallic photovoltaics: A new and versatile
1155 approach for harvesting solar energy using conjugated polymetallaynes. *Acc*
1156 *Chem Res* 2010;43:1246–56. <https://doi.org/10.1021/ar1000378>.
- 1157 [11] Pinel P, Cruickshank CA, Beausoleil-Morrison I, Wills A. A review of available
1158 methods for seasonal storage of solar thermal energy in residential
1159 applications. *Renew Sustain Energy Rev* 2011;15:3341–59.
1160 <https://doi.org/10.1016/j.rser.2011.04.013>.
- 1161 [12] El-Khouly ME, El-Mohsnawy E, Fukuzumi S. Solar energy conversion: From
1162 natural to artificial photosynthesis. *J Photochem Photobiol C Photochem Rev*
1163 2017;31:36–83. <https://doi.org/10.1016/j.jphotochemrev.2017.02.001>.
- 1164 [13] Wang YC, Liu XY, Wang XX, Cao MS. Metal-organic frameworks based
1165 photocatalysts: Architecture strategies for efficient solar energy conversion.
1166 *Chem Eng J* 2021;419. <https://doi.org/10.1016/j.cej.2021.129459>.
- 1167 [14] Li J, Slassi A, Han X, Cornil D, Ha-Thi MH, Pino T, et al. Tuning the Electronic
1168 Bandgap of Graphdiyne by H-Substitution to Promote Interfacial Charge
1169 Carrier Separation for Enhanced Photocatalytic Hydrogen Production. *Adv*
1170 *Funct Mater* 2021;31. <https://doi.org/10.1002/adfm.202100994>.
- 1171 [15] Xu Q, Knezevic M, Laachachi A, Franger S, Colbeau-Justin C, Ghazzal MN.
1172 Insight into Interfacial Charge Transfer during Photocatalytic H₂ Evolution
1173 through Fe, Ni, Cu and Au Embedded in a Mesoporous TiO₂@SiO₂ Core-
1174 shell. *ChemCatChem* 2022. <https://doi.org/10.1002/cctc.202200102>.
- 1175 [16] Cui Z, Zhao M, Li S, Wang J, Xu Y, Ghazzal MN, et al. Facile Vacuum
1176 Annealing of TiO₂ with Ethanol-Induced Enhancement of Its Photocatalytic
1177 Performance under Visible Light. *Ind Eng Chem Res* 2022;61:14455–61.
1178 <https://doi.org/10.1021/acs.iecr.2c01842>.
- 1179 [17] Wang C, Li J, Paineau E, Remita H, Ghazzal MN. Pt Atomically Dispersed in
1180 Black TiO₂-x/CuxO with Chiral-Like Nanostructure for Visible-Light H₂
1181 Generation. *Sol RRL* 2023;7. <https://doi.org/10.1002/solr.202200929>.
- 1182 [18] Tanji K, Zouheir M, Hachhach M, Ahmoum H, Jellal I, Masaoudi H El, et al.
1183 Design and simulation of a photocatalysis reactor for rhodamine B degradation
1184 using cobalt-doped ZnO film. *React Kinet Mech Catal* 2021;134:1017–1038.
1185 <https://doi.org/https://doi.org/10.1007/s11144-021-02116-3>.
- 1186 [19] Fahoul Y, Tanji K, Zouheir M, Mrabet I El, Naciri Y, Hsini A, et al. Novel River
1187 Sediment@ZnO@Co nanocomposite for photocatalytic degradation and COD
1188 reduction of crystal violet under visible light. *J Mol Struct* 2022;1253:132298.
1189 <https://doi.org/10.1016/j.molstruc.2021.132298>.
- 1190 [20] Tanji K, Zouheir M, Naciri Y, Ahmoum H, Hsini A, Mertah O, et al. Visible light
1191 photodegradation of blue basic 41 using cobalt doped ZnO: Box–Behnken
1192 optimization and DFT calculation. *J Iran Chem Soc* 2022;1–16.
1193 <https://doi.org/10.1007/s13738-022-02496-w>.

- 1194 [21] Hamza MA, El-Sayed A, El-Shazly AN, Elmahgary MG. Efficient utilization of
 1195 ceramic waste (cyclone dust waste) for enhancing the photocatalytic
 1196 performance of TiO₂ nanoparticles toward Rhodamine B photodegradation. *J*
 1197 *Clean Prod* 2024;434:140341. <https://doi.org/10.1016/j.jclepro.2023.140341>.
- 1198 [22] Hamza MA, Rizk SA, Ezz-Elregal E-EM, El-Rahman SAA, Ramadan SK,
 1199 Abou- Gamra ZM. Photosensitization of TiO₂ microspheres by novel
 1200 Quinazoline-derivative as visible-light-harvesting antenna for enhanced
 1201 Rhodamine B photodegradation. *Sci Rep* 2023;13:12929.
 1202 <https://doi.org/10.1038/s41598-023-38497-9>.
- 1203 [23] Hamza MA, Abd El-Rahman SA, Abou-Gamra ZM. Facile one-pot solid-state
 1204 fabrication of a novel binary nanocomposite of commercial ZnO and
 1205 commercial PbCrO₄ with enhanced photocatalytic degradation of Rhodamine
 1206 B dye. *Opt Mater (Amst)* 2022;124:111987.
 1207 <https://doi.org/10.1016/j.optmat.2022.111987>.
- 1208 [24] Hashem EM, Hamza MA, El-Shazly AN, Abd El-Rahman SA, El-Tanany EM,
 1209 Mohamed RT, et al. Novel Z-Scheme/Type-II CdS@ZnO/g-C₃N₄ ternary
 1210 nanocomposites for the durable photodegradation of organics: Kinetic and
 1211 mechanistic insights. *Chemosphere* 2021;277:128730.
 1212 <https://doi.org/10.1016/j.chemosphere.2020.128730>.
- 1213 [25] Tanji K, El Mrabet I, Fahoul Y, Soussi A, Belghiti M, Jellal I, et al. Experimental
 1214 and theoretical investigation of enhancing the photocatalytic activity of Mg
 1215 doped ZnO for nitrophenol degradation. *React Kinet Mech Catal*
 1216 2023;136:1125–42. <https://doi.org/10.1007/s11144-023-02385-0>.
- 1217 [26] Zhang Y, Shi Z, Gu Z, Iijima S. Structure modification of single-wall carbon
 1218 nanotubes. *Carbon N Y* 2000;38:2055–9.
 1219 [https://doi.org/https://doi.org/10.1016/S0008-6223\(00\)00047-6](https://doi.org/https://doi.org/10.1016/S0008-6223(00)00047-6).
- 1220 [27] Ge M, Li Q, Cao C, Huang J, Li S, Zhang S, et al. One-dimensional TiO₂
 1221 Nanotube Photocatalysts for Solar Water Splitting. *Adv Sci* 2017;4.
 1222 <https://doi.org/10.1002/advs.201600152>.
- 1223 [28] Ju L, Dai Y, Wei W, Li M, Liang Y, Huang B. One-dimensional cadmium
 1224 sulphide nanotubes for photocatalytic water splitting. *Phys Chem Chem Phys*
 1225 2018;20:1904–13. <https://doi.org/10.1039/c7cp06568j>.
- 1226 [29] Dong X, Yang P, Liu Y, Jia C, Wang D, Wang J, et al. Morphology evolution of
 1227 one-dimensional ZnO nanostructures towards enhanced photocatalysis
 1228 performance. *Ceram Int* 2016;42:518–26.
 1229 <https://doi.org/10.1016/j.ceramint.2015.08.140>.
- 1230 [30] Zhukovskii YF, Piskunov S, Lisovski O, Bocharov D, Evarestov RA. Doped 1D
 1231 Nanostructures of Transition-metal Oxides: First-principles Evaluation of
 1232 Photocatalytic Suitability. *Isr J Chem* 2017;57:461–76.
 1233 <https://doi.org/10.1002/ijch.201600099>.
- 1234 [31] Weng B, Liu S, Zhang N, Tang ZR, Xu YJ. A simple yet efficient visible-light-
 1235 driven CdS nanowires-carbon nanotube 1D-1D nanocomposite photocatalyst.
 1236 *J Catal* 2014;309:146–55. <https://doi.org/10.1016/j.jcat.2013.09.013>.
- 1237 [32] Zhang G, Guan Z, Yang J, Li Q, Zhou Y, Zou Z. Metal Sulfides for
 1238 Photocatalytic Hydrogen Production: Current Development and Future
 1239 Challenges. *Sol RRL* 2022;6:1–15. <https://doi.org/10.1002/solr.202200587>.
- 1240 [33] Liu Z, Zhang X, Jiang Z, Chen HS, Yang P. Phosphorus and sulphur co-doping
 1241 of g-C₃N₄ nanotubes with tunable architectures for superior photocatalytic H₂
 1242 evolution. *Int J Hydrogen Energy* 2019;44:20042–55.
 1243 <https://doi.org/10.1016/j.ijhydene.2019.06.037>.
- 1244 [34] Huang K, Li C, Zhang X, Wang L, Wang W, Meng X. Self-assembly synthesis

- 1245 of phosphorus-doped tubular g-C₃N₄/Ti₃C₂ MXene Schottky junction for
 1246 boosting photocatalytic hydrogen evolution. *Green Energy Environ* 2021.
 1247 <https://doi.org/10.1016/j.gee.2021.03.011>.
- 1248 [35] Kumar S, Sharma M, Powar S, Kabachkov EN, Vaish R. Impact of remnant
 1249 surface polarization on photocatalytic and antibacterial performance of BaTiO
 1250 3. *J Eur Ceram Soc* 2019;39:2915–22.
 1251 <https://doi.org/10.1016/j.jeurceramsoc.2019.03.029>.
- 1252 [36] Ali SS, Qazi IA, Arshad M, Khan Z, Voice TC, Mehmood CT. Photocatalytic
 1253 degradation of low density polyethylene (LDPE) films using titania nanotubes.
 1254 *Environ Nanotechnology, Monit Manag* 2016;5:44–53.
 1255 <https://doi.org/10.1016/j.enmm.2016.01.001>.
- 1256 [37] Sun L, Li J, Wang C, Li S, Lai Y, Chen H, et al. Ultrasound aided
 1257 photochemical synthesis of Ag loaded TiO₂ nanotube arrays to enhance
 1258 photocatalytic activity. *J Hazard Mater* 2009;171:1045–50.
 1259 <https://doi.org/10.1016/j.jhazmat.2009.06.115>.
- 1260 [38] Das R, Abd Hamid SB, Ali ME, Ismail AF, Annur MSM, Ramakrishna S.
 1261 Multifunctional carbon nanotubes in water treatment: The present, past and
 1262 future. *Desalination* 2014;354:160–79.
 1263 <https://doi.org/10.1016/j.desal.2014.09.032>.
- 1264 [39] Liu X, Wang M, Zhang S, Pan B. Application potential of carbon nanotubes in
 1265 water treatment: A review. *J Environ Sci (China)* 2013;25:1263–80.
 1266 [https://doi.org/10.1016/S1001-0742\(12\)60161-2](https://doi.org/10.1016/S1001-0742(12)60161-2).
- 1267 [40] Zhang X, Zhang X, Yang P, Ping Jiang S. Transition metals decorated g-
 1268 C₃N₄/N-doped carbon nanotube catalysts for water splitting: A review. *J*
 1269 *Electroanal Chem* 2021;895. <https://doi.org/10.1016/j.jelechem.2021.115510>.
- 1270 [41] Lvov Y, Wang W, Zhang L, Fakhrullin R. Halloysite Clay Nanotubes for
 1271 Loading and Sustained Release of Functional Compounds. *Adv Mater*
 1272 2016;28:1227–50. <https://doi.org/10.1002/adma.201502341>.
- 1273 [42] Paineau E, Bihannic I, Baravian C, Philippe AM, Davidson P, Levitz P, et al.
 1274 Aqueous suspensions of natural swelling clay minerals. 1. structure and
 1275 electrostatic interactions. *Langmuir* 2011;27:5562–73.
 1276 <https://doi.org/10.1021/la2001255>.
- 1277 [43] Paineau E, Rouzière S, Monet G, Diogo CC, Morfin I, Launois P. Role of initial
 1278 precursors on the liquid-crystalline phase behavior of synthetic
 1279 aluminogermanate imogolite nanotubes. *J Colloid Interface Sci* 2020;580:275–
 1280 85. <https://doi.org/10.1016/j.jcis.2020.07.036>.
- 1281 [44] Serra M, Arenal R, Tenne R. An overview of the recent advances in inorganic
 1282 nanotubes. *Nanoscale* 2019;11:8073–90. <https://doi.org/10.1039/c9nr01880h>.
- 1283 [45] Liu Q, Peng H, Tian X, Guo J. Synthesis of chrysotile based nanocomposites
 1284 for tuning band gap and photocatalytic property. *Appl Clay Sci* 2020;199.
 1285 <https://doi.org/10.1016/j.clay.2020.105885>.
- 1286 [46] Liu M, Chang Y, Yang J, You Y, He R, Chen T, et al. Functionalized halloysite
 1287 nanotube by chitosan grafting for drug delivery of curcumin to achieve
 1288 enhanced anticancer efficacy. *J Mater Chem B* 2016;4:2253–63.
 1289 <https://doi.org/10.1039/c5tb02725j>.
- 1290 [47] Luo Q, Peng H, Tian X, Guo J. Facile synthesis and characterization of
 1291 Chrysotile/SnO₂ nanocomposite for enhanced photocatalytic properties. *Appl*
 1292 *Organomet Chem* 2020;34. <https://doi.org/10.1002/aoc.5356>.
- 1293 [48] Joussein, E. Petit, S.Churchman, J.Theng, B. Righi, D. And Delvaux B.
 1294 Halloysite clay minerals- a review. *Clay Miner* 2005;40:383–426.
 1295 <https://doi.org/https://doi.org/10.1180/0009855054040180>.

- 1296 [49] Liu M, Chang Y, Yang J, You Y, He R, Chen T, et al. Functionalized halloysite
1297 nanotube by chitosan grafting for drug delivery of curcumin to achieve
1298 enhanced anticancer efficacy. *J Mater Chem B* 2016;4:2253–63.
1299 <https://doi.org/10.1039/c5tb02725j>.
- 1300 [50] Yuan P, Tan D, Annabi-Bergaya F. Properties and applications of halloysite
1301 nanotubes: Recent research advances and future prospects. *Appl Clay Sci*
1302 2015;112–113:75–93. <https://doi.org/10.1016/j.clay.2015.05.001>.
- 1303 [51] Gonza RI, Ram R, Rogan J, Valdivia JA, Munoz F, Valencia F, et al. Model for
1304 Self-Rolling of an Aluminosilicate Sheet into a Single- Walled Imogolite
1305 Nanotube. *J Phys Chem C* 2014;118:28227.
1306 <https://doi.org/https://doi.org/10.1021/jp508637q>.
- 1307 [52] P. D. G. Cradwick, V. C. Farmer, J. D. Russel, C. R. Masson KW& NY.
1308 Imogolite, a Hydrated Aluminium Silicate of Tubular Structure. *Nat Phys Sci*
1309 1972;240:187–9. <https://doi.org/https://doi.org/10.1038/physci240187a0>.
- 1310 [53] Paineau E. Imogolite nanotubes: A flexible nanoplatform with multipurpose
1311 applications. *Appl Sci* 2018;8. <https://doi.org/10.3390/app8101921>.
- 1312 [54] D'Angelo A, Paineau E, Rouzière S, Elkaim É, Goldmann C, Toquer D, et al.
1313 The atomic structure of imogolite nanotubes: A 50 years old issue
1314 reinvestigated by X-ray scattering experiments and molecular dynamics
1315 simulations. *Appl Clay Sci* 2023;242:107043.
1316 <https://doi.org/10.1016/j.clay.2023.107043>.
- 1317 [55] King TVV, Clark RN. Spectral characteristics of chlorites and Mg-serpentine
1318 using high- resolution reflectance spectroscopy. *J Geophys Res* 1989;94.
1319 <https://doi.org/10.1029/jb094ib10p13997>.
- 1320 [56] Krasilin AA. energy modeling of competition between tubular and platy
1321 morphologies of chrysotile and halloysite layers. *Clays Clay Miner*
1322 2020;68:436–45. <https://doi.org/10.1007/s42860-020-00086-6>.
- 1323 [57] Teobaldi G, Beglitis NS, Fisher AJ, Zerbetto F, Hofer WA. Hydroxyl vacancies
1324 in single-walled aluminosilicate and aluminogermanate nanotubes. *J Phys*
1325 *Condens Matter* 2009;21. <https://doi.org/10.1088/0953-8984/21/19/195301>.
- 1326 [58] Guimarães L, Enyashin AN, Frenzel J, Heine T, Duarte HA, Seifert G.
1327 Imogolite nanotubes: Stability, electronic, and mechanical properties. *ACS*
1328 *Nano* 2007;1:362–8. <https://doi.org/10.1021/nn700184k>.
- 1329 [59] Piperno S, Kaplan-Ashiri I, Cohen SR, Popovitz-Biro R, Wagner HD, Tenne R,
1330 et al. Characterization of geoinspired and synthetic chrysotile nanotubes by
1331 atomic force microscopy and transmission electron microscopy. *Adv Funct*
1332 *Mater* 2007;17:3332–8. <https://doi.org/10.1002/adfm.200700278>.
- 1333 [60] Lecouvet B, Horion J, D'Haese C, Bailly C, Nysten B. Elastic modulus of
1334 halloysite nanotubes. *Nanotechnology* 2013;24. <https://doi.org/10.1088/0957-4484/24/10/105704>.
- 1336 [61] S.Rouzière, V. Balédent, E. Paineau, E. Elkaim, T. Bizien, L. Nataf, Y. Pan
1337 and PL. Compressibility and Structural Transformations of Aluminogermanate
1338 Imogolite Nanotubes under Hydrostatic Pressure. *Inorg Chem* 2023;62:957-
1339 966. <https://doi.org/https://doi.org/10.1021/acs.inorgchem.2c03798>.
- 1340 [62] Xiao M, Wang Z, Lyu M, Luo B, Wang S, Liu G, et al. Hollow Nanostructures
1341 for Photocatalysis: Advantages and Challenges. *Adv Mater* 2019;31.
1342 <https://doi.org/10.1002/adma.201801369>.
- 1343 [63] Alvarez-Ramírez F. First principles studies of Fe-containing aluminosilicate
1344 and aluminogermanate nanotubes. *J Chem Theory Comput* 2009;5:3224–31.
1345 <https://doi.org/10.1021/ct9004992>.
- 1346 [64] Zhao M, Xia Y, Mei L. Energetic minimum structures of imogolite nanotubes: A

- 1347 first-principles prediction. *J Phys Chem C* 2009;113:14834–7.
1348 <https://doi.org/10.1021/jp9056169>.
- 1349 [65] Poli E, Elliott JD, Ratcliff LE, Andrinopoulos L, Dziedzic J, Hine NDM, et al.
1350 The potential of imogolite nanotubes as (co-)photocatalysts: A linear-scaling
1351 density functional theory study. *J Phys Condens Matter* 2016;28:074003.
1352 <https://doi.org/10.1088/0953-8984/28/7/074003>.
- 1353 [66] Pignié MC, Shcherbakov V, Charpentier T, Moskura M, Carteret C, Denisov S,
1354 et al. Confined water radiolysis in aluminosilicate nanotubes: The importance
1355 of charge separation effects. *Nanoscale* 2021;13:3092–105.
1356 <https://doi.org/10.1039/d0nr08948f>.
- 1357 [67] Katsumata K ichi, Hou X, Sakai M, Nakajima A, Fujishima A, Matsushita N, et
1358 al. Visible-light-driven photodegradation of acetaldehyde gas catalyzed by
1359 aluminosilicate nanotubes and Cu(II)-grafted TiO₂ composites. *Appl Catal B*
1360 *Environ* 2013;138–139:243–52. <https://doi.org/10.1016/j.apcatb.2013.03.004>.
- 1361 [68] Papoulis D, Komarneni S, Panagiotaras D, Stathatos E, Toli D, Christoforidis
1362 KC, et al. Halloysite-TiO₂ nanocomposites: Synthesis, characterization and
1363 photocatalytic activity. *Appl Catal B Environ* 2013;132–133:416–22.
1364 <https://doi.org/10.1016/j.apcatb.2012.12.012>.
- 1365 [69] Monteiro RRC, de Oliveira ALB, de Menezes FL, de Souza MCM, Fachine
1366 PBA, dos Santos JCS. Improvement of enzymatic activity and stability of lipase
1367 A from *Candida antarctica* onto halloysite nanotubes with Taguchi method for
1368 optimized immobilization. *Appl Clay Sci* 2022;228.
1369 <https://doi.org/10.1016/j.clay.2022.106634>.
- 1370 [70] Barebita H, Naciri Y, Ferraa S, Nimour A, Guedira T. Investigation of structural
1371 and photocatalytic behavior of Bi₁₃B₁-2xV_xP_xO₂₀. 95+ 2x (0 ≤ x ≤ 0.5). *Solid*
1372 *State Sci* 2020;108:106389.
1373 <https://doi.org/https://doi.org/10.1016/j.solidstatesciences.2020.106389>.
- 1374 [71] Naciri Y, Hsini A, Bouziani A, Tanji K, El Ibrahim B, Ghazzal MN, et al. Z-
1375 scheme WO₃/PANI heterojunctions with enhanced photocatalytic activity
1376 under visible light: A depth experimental and DFT studies. *Chemosphere*
1377 2022;292:133468. <https://doi.org/10.1016/j.chemosphere.2021.133468>.
- 1378 [72] Naciri Y, Hsini A, Bouziani A, Djellabi R, Ajmal Z, Laabd M, et al.
1379 Photocatalytic oxidation of pollutants in gas-phase via Ag₃PO₄-based
1380 semiconductor photocatalysts: Recent progress, new trends, and future
1381 perspectives. *Crit Rev Environ Sci Technol* 2022;52:2339–82.
1382 <https://doi.org/10.1080/10643389.2021.1877977>.
- 1383 [73] Ran J, Jaroniec M, Qiao SZ. Cocatalysts in Semiconductor-based
1384 Photocatalytic CO₂ Reduction: Achievements, Challenges, and Opportunities.
1385 *Adv Mater* 2018;30. <https://doi.org/10.1002/adma.201704649>.
- 1386 [74] Zhou P, Yu J, Jaroniec M. All-solid-state Z-scheme photocatalytic systems.
1387 *Adv Mater* 2014;26:4920–35. <https://doi.org/10.1002/adma.201400288>.
- 1388 [75] Rahman MZ, Kibria MG, Mullins CB. Metal-free photocatalysts for hydrogen
1389 evolution. *Chem Soc Rev* 2020;49:1887–931.
1390 <https://doi.org/10.1039/c9cs00313d>.
- 1391 [76] Kudo A, Miseki Y. Heterogeneous photocatalyst materials for water splitting.
1392 *Chem Soc Rev* 2009;38:253–78. <https://doi.org/10.1039/b800489g>.
- 1393 [77] Wang Q, Domen K. Particulate Photocatalysts for Light-Driven Water Splitting:
1394 Mechanisms, Challenges, and Design Strategies. *Chem Rev* 2020;120:919–
1395 85. <https://doi.org/10.1021/acs.chemrev.9b00201>.
- 1396 [78] Naciri Y, Hsini A, Ajmal Z, Navío JA, Bakiz B, Albourine A, et al. Recent
1397 progress on the enhancement of photocatalytic properties of BiPO₄ using π–

- 1398 conjugated materials. *Adv Colloid Interface Sci* 2020;280.
 1399 <https://doi.org/10.1016/j.cis.2020.102160>.
- 1400 [79] Naciri Y, Hsini A, Ahdour A, Akhsassi B, Fritah kamal, Ajmal Z, et al. Recent
 1401 advances of bismuth titanate based photocatalysts engineering for enhanced
 1402 organic contaminates oxidation in water: A review. *Chemosphere* 2022;300.
 1403 <https://doi.org/10.1016/j.chemosphere.2022.134622>.
- 1404 [80] Fahoul Y, Tanji K, González Díaz OM, Quesada-Cabrera R, Naciri Y, El
 1405 Mrabet I, et al. Development of a new CoS-Supported ZnAl₂O₄ catalyst for the
 1406 visible photodegradation of a basic textile dye from water. *Opt Mater (Amst)*
 1407 2023;143. <https://doi.org/10.1016/j.optmat.2023.114148>.
- 1408 [81] Kubacka A, Fernández-García M, Colón G. Advanced nanoarchitectures for
 1409 solar photocatalytic applications. *Chem Rev* 2012;112:1555–614.
 1410 <https://doi.org/10.1021/cr100454n>.
- 1411 [82] Wei K, Faraj Y, Yao G, Xie R, Lai B. Strategies for improving perovskite
 1412 photocatalysts reactivity for organic pollutants degradation: A review on recent
 1413 progress. *Chem Eng J* 2021;414. <https://doi.org/10.1016/j.cej.2021.128783>.
- 1414 [83] Hu C, Tu S, Tian N, Ma T, Zhang Y, Huang H. Photocatalysis Enhanced by
 1415 External Fields. *Angew Chemie - Int Ed* 2021;60:16309–28.
 1416 <https://doi.org/10.1002/anie.202009518>.
- 1417 [84] Mimouni I, Yahya M, Bouziani A, Naciri Y, Maarouf F ezzahra, Alaoui El
 1418 Belghiti M, et al. Iron phosphate for photocatalytic removal of Ibuprofen from
 1419 aqueous media under sun-like irradiation. *J Photochem Photobiol A Chem*
 1420 2022;433:114170. <https://doi.org/10.1016/j.jphotochem.2022.114170>.
- 1421 [85] Ajmal Z, Naciri Y, Ahmad M, Hsini A, Bouziani A, Laabd M, et al. Use of
 1422 conductive polymer-supported oxide-based photocatalysts for efficient VOCs &
 1423 SVOCs removal in gas/liquid phase. *J Environ Chem Eng* 2023;11:108935.
 1424 <https://doi.org/10.1016/j.jece.2022.108935>.
- 1425 [86] Akhsassi B, Naciri Y, Bouddouch A, Bakiz B, Taoufyq A, Villain S, et al. Facile
 1426 novel acid coprecipitation synthesis of BiPO₄ polymorphs: Enhanced
 1427 photocatalytic degradation of the antibiotic AMX and the dyes RhB, MB and
 1428 MO. *Opt Mater (Amst)* 2023;137:113575.
 1429 <https://doi.org/10.1016/j.optmat.2023.113575>.
- 1430 [87] Sadjadi S. Halloysite-based hybrids/composites in catalysis. *Appl Clay Sci*
 1431 2020;189. <https://doi.org/10.1016/j.clay.2020.105537>.
- 1432 [88] Mishra A, Mehta A, Basu S. Clay supported TiO₂ nanoparticles for
 1433 photocatalytic degradation of environmental pollutants: A review. *J Environ*
 1434 *Chem Eng* 2018;6:6088–107. <https://doi.org/10.1016/j.jece.2018.09.029>.
- 1435 [89] Li C, Zhu N, Yang S, He X, Zheng S, Sun Z, et al. A review of clay based
 1436 photocatalysts: Role of phyllosilicate mineral in interfacial assembly,
 1437 microstructure control and performance regulation. *Chemosphere*
 1438 2021;273:129723. <https://doi.org/10.1016/j.chemosphere.2021.129723>.
- 1439 [90] Zhu S, Wang D. Photocatalysis: Basic principles, diverse forms of
 1440 implementations and emerging scientific opportunities. *Adv Energy Mater*
 1441 2017;7:1–24. <https://doi.org/10.1002/aenm.201700841>.
- 1442 [91] Xiao FX, Miao J, Tao HB, Hung SF, Wang HY, Yang H Bin, et al. One-
 1443 dimensional hybrid nanostructures for heterogeneous photocatalysis and
 1444 photoelectrocatalysis. *Small* 2015;11:2115–31.
 1445 <https://doi.org/10.1002/sml.201402420>.
- 1446 [92] Li L, Zhao C, Zhang L, Zhu Y. γ -GeSe nanotubes: A one-dimensional
 1447 semiconductor with high carrier mobility potential for photocatalytic water
 1448 splitting. *J Mater Chem C* 2021;9:15158–64.

- 1449 <https://doi.org/10.1039/d1tc04204a>.
- 1450 [93] Jiang D, Jing H, Liu Z, Jia C, Liu Q. Natural Halloysite Nanotube as a Spatially
1451 Confined Nanoreactor for Improving Photocatalytic Performance. *J Phys Chem*
1452 *C* 2021;125:15316–23. <https://doi.org/10.1021/acs.jpcc.1c04065>.
- 1453 [94] Zhu K, Neale NR, Miedaner A, Frank AJ. Enhanced charge-collection
1454 efficiencies and light scattering in dye-sensitized solar cells using oriented
1455 TiO₂ nanotubes arrays. *Nano Lett* 2007;7:69–74.
1456 <https://doi.org/10.1021/nl062000o>.
- 1457 [95] Macak JM, Zlamal M, Krysa J, Schmuki P. Self-organized TiO₂ nanotube
1458 layers as highly efficient photocatalysts. *Small* 2007;3:300–4.
1459 <https://doi.org/10.1002/sml.200600426>.
- 1460 [96] Patra S, Schaming D, Picot P, Pignié MC, Brubach JB, Sicard L, et al.
1461 Inorganic nanotubes with permanent wall polarization as dual photo-reactors
1462 for wastewater treatment with simultaneous fuel production. *Environ Sci Nano*
1463 2021;8:2523–41. <https://doi.org/10.1039/d1en00405k>.
- 1464 [97] Das S, Jana S. A tubular nanoreactor directing the formation of in situ iron
1465 oxide nanorods with superior photocatalytic activity. *Environ Sci Nano*
1466 2017;4:596–603. <https://doi.org/10.1039/c6en00570e>.
- 1467 [98] Zsirka B, Vágvölgyi V, Horváth E, Juzsakova T, Fónagy O, Szabó-bárdos E, et
1468 al. Halloysite-Zinc Oxide Nanocomposites as Potential Photocatalysts.
1469 *Minerals* 2022;12. <https://doi.org/10.3390/min12040476>.
- 1470 [99] Mishra G, Mukhopadhyay M. TiO₂ decorated functionalized halloysite
1471 nanotubes (TiO₂ @HNTs) and photocatalytic PVC membranes synthesis,
1472 characterization and its application in water treatment. *Sci Rep* 2019;9:1–17.
1473 <https://doi.org/10.1038/s41598-019-40775-4>.
- 1474 [100] Pignié MC, Patra S, Huart L, Milosavljević AR, Renault JP, Leroy J, et al.
1475 Experimental determination of the curvature-induced intra-wall polarization of
1476 inorganic nanotubes. *Nanoscale* 2021;13:19650–62.
1477 <https://doi.org/10.1039/d1nr06462b>.
- 1478 [101] Chen F, Huang H, Guo L, Zhang Y, Ma T. The Role of Polarization in
1479 Photocatalysis. *Angew Chemie - Int Ed* 2019;58:10061–73.
1480 <https://doi.org/10.1002/anie.201901361>.
- 1481 [102] Ghicov A, Schmuki P. Self-ordering electrochemistry: A review on growth and
1482 functionality of TiO₂ nanotubes and other self-aligned MO_x structures. *Chem*
1483 *Commun* 2009:2791–808. <https://doi.org/10.1039/b822726h>.
- 1484 [103] Zhang P, Lou XW (David). Design of Heterostructured Hollow Photocatalysts
1485 for Solar-to-Chemical Energy Conversion. *Adv Mater* 2019;31:1–18.
1486 <https://doi.org/10.1002/adma.201900281>.
- 1487 [104] Wong LW, Goh CBS, Pasbakhsh P, Tan JBL. Natural hollow clay nanotubes
1488 and their applications as polymer nanocomposites in tissue engineering. *J Sci*
1489 *Adv Mater Devices* 2022;7. <https://doi.org/10.1016/j.jsamd.2022.100431>.
- 1490 [105] Ng KM, Lau YTR, Chan CM, Weng LT, Wu J. Surface studies of halloysite
1491 nanotubes by XPS and ToF-SIMS. *Surf Interface Anal* 2011;43:795–802.
1492 <https://doi.org/10.1002/sia.3627>.
- 1493 [106] Cavallaro G, Lazzara G, Konnova S, Fakhrullin R, Lvov Y. Composite films of
1494 natural clay nanotubes with cellulose and chitosan. *Green Mater* 2014;2:232–
1495 42. <https://doi.org/10.1680/gmat.14.00014>.
- 1496 [107] Abdullayev E, Lvov Y. Halloysite clay nanotubes for controlled release of
1497 protective agents. *J Nanosci Nanotechnol* 2011;11:10007–26.
1498 <https://doi.org/10.1166/jnn.2011.5724>.
- 1499 [108] Cavallaro G, Lazzara G, Pignon F, Chiappisi L, Paineau E. Effect of Polymer

- 1500 Length on the Adsorption onto Aluminogermanate Imogolite Nanotubes.
 1501 Langmuir 2021;37:9858–64. <https://doi.org/10.1021/acs.langmuir.1c01549>.
- 1502 [109] Luo P, Zhao Y, Zhang B, Liu J, Yang Y, Liu J. Study on the adsorption of
 1503 Neutral Red from aqueous solution onto halloysite nanotubes. Water Res
 1504 2010;44:1489–97. <https://doi.org/10.1016/j.watres.2009.10.042>.
- 1505 [110] Sadjadi S. Halloysite-based hybrids/composites in catalysis. Appl Clay Sci
 1506 2020;189:105537. <https://doi.org/10.1016/j.clay.2020.105537>.
- 1507 [111] Lazzara G, Cavallaro G, Panchal A, Fakhrullin R, Stavitskaya A, Vinokurov V,
 1508 et al. An assembly of organic-inorganic composites using halloysite clay
 1509 nanotubes. Curr Opin Colloid Interface Sci 2018;35:42–50.
 1510 <https://doi.org/10.1016/j.cocis.2018.01.002>.
- 1511 [112] Lisuzzo L, Cavallaro G, Lazzara G, Milioto S, Parisi F, Stetsyshyn Y. Stability
 1512 of halloysite, imogolite, and boron nitride nanotubes in solvent media. Appl Sci
 1513 2018;8. <https://doi.org/10.3390/app8071068>.
- 1514 [113] Ferrante F, Armata N, Lazzara G. Modeling of the Halloysite Spiral Nanotube.
 1515 J Phys Chem C 2015;119:16700–7. <https://doi.org/10.1021/acs.jpcc.5b04281>.
- 1516 [114] Joo Y, Joo JH, Jeon Y, Lee SU, Sohn D. Opening and blocking the inner-pores
 1517 of halloysite. Chem Commun 2013;49:4519–21.
 1518 <https://doi.org/10.1039/c3cc40465j>.
- 1519 [115] Atyaksheva LF, Kasyanov IA. Halloysite, Natural Aluminosilicate Nanotubes:
 1520 Structural Features and Adsorption Properties (A Review). Pet Chem
 1521 2021;61:932–50. <https://doi.org/10.1134/S0965544121080119>.
- 1522 [116] Gianni E, Pšenička M, Macková K, Scholtzová E, Jankovič Ľ, Mareš M, et al.
 1523 New detail insight into Halloysite structure: Mechanism behind nanotubular
 1524 morphology described by density functional theory and molecular dynamics
 1525 supported by experiments. J Mol Struct 2023;1287.
 1526 <https://doi.org/10.1016/j.molstruc.2023.135639>.
- 1527 [117] Zhang Y, Fu L, Shu Z, Yang H, Tang A, Jiang T. Substitutional Doping for
 1528 Aluminosilicate Mineral and Superior Water Splitting Performance. Nanoscale
 1529 Res Lett 2017;12. <https://doi.org/10.1186/s11671-017-2192-8>.
- 1530 [118] Yoshinaga N, Aomine S. Imogolite in some ando soils. Soil Sci Plant Nutr
 1531 1962;8:22–9. <https://doi.org/10.1080/00380768.1962.10430993>.
- 1532 [119] Paineau E, Launois P. Nanomaterials from imogolite: Structure, properties,
 1533 and functional materials. Nanomater. from Clay Miner. A New Approach to
 1534 Green Funct. Mater., Elsevier; 2019, p. 257–84. <https://doi.org/10.1016/B978-0-12-814533-3.00005-3>.
- 1536 [120] Garrone E, Bonelli B. Imogolite for Catalysis and Adsorption. Dev. Clay Sci.,
 1537 vol. 7, Elsevier B.V.; 2016, p. 672–707. <https://doi.org/10.1016/B978-0-08-100293-3.00025-X>.
- 1539 [121] Konduri S, Mukherjee S, Nair S. Strain energy minimum and vibrational
 1540 properties of single-walled aluminosilicate nanotubes. Phys Rev B - Condens
 1541 Matter Mater Phys 2006;74:1–4. <https://doi.org/10.1103/PhysRevB.74.033401>.
- 1542 [122] Monet G, Amara MS, Rouzière S, Paineau E, Chai Z, Elliott JD, et al.
 1543 Structural resolution of inorganic nanotubes with complex stoichiometry. Nat
 1544 Commun 2018;9. <https://doi.org/10.1038/s41467-018-04360-z>.
- 1545 [123] Paineau E, Monet G, Peyre V, Goldmann C, Rouzière S, Launois P. Colloidal
 1546 Stability of Imogolite Nanotube Dispersions: A Phase Diagram Study.
 1547 Langmuir 2019;35:12451–9. <https://doi.org/10.1021/acs.langmuir.9b01922>.
- 1548 [124] Farmer VC, Fraser AR, Tait. Synthesis of Imogolite: A Tubular Aluminium
 1549 Silicate Polymer. 1977. <https://doi.org/https://doi.org/10.1039/C39770000462>.
- 1550 [125] Farmer VC, Adams MJ, Fraser AR, Palmieri F. Synthetic imogolite: properties,

- 1551 synthesis and possible applications. *Clay Miner* 1983;18:459–72.
 1552 <https://doi.org/10.1180/claymin.1983.018.4.11>.
- 1553 [126] Bursill LA, Peng JL, Bourgeois LN. Imogolite: An aluminosilicate nanotube
 1554 material. *Philos Mag A Phys Condens Matter, Struct Defects Mech Prop*
 1555 2000;80:105–17. <https://doi.org/10.1080/01418610008212043>.
- 1556 [127] Li L, Xia Y, Zhao M, Song C, Li J, Liu X. The electronic structure of a single-
 1557 walled aluminosilicate nanotube. *Nanotechnology* 2008;19.
 1558 <https://doi.org/10.1088/0957-4484/19/17/175702>.
- 1559 [128] Alvarez-Ramírez F. Ab initio simulation of the structural and electronic
 1560 properties of aluminosilicate and aluminogermanate nanotubes with imogolite-
 1561 like structure. *Phys Rev B - Condens Matter Mater Phys* 2007;76.
 1562 <https://doi.org/10.1103/PhysRevB.76.125421>.
- 1563 [129] Kato K, Inukai K, Fujikura K, Kasuga T. Effective encapsulation of laccase in
 1564 an aluminium silicate nanotube hydrogel. *New J Chem* 2014;38:3591–9.
 1565 <https://doi.org/10.1039/c4nj00080c>.
- 1566 [130] Wada S-I, Wada K. Effects of substitution of germanium. vol. 30. 1982.
 1567 <https://doi.org/https://doi.org/10.1346/CCMN.1982.0300206>.
- 1568 [131] Paineau E, Krapf MEM, Amara MS, Matskova N V., Dozov I, Rouzière S, et al.
 1569 A liquid-crystalline hexagonal columnar phase in highly-dilute suspensions of
 1570 imogolite nanotubes. *Nat Commun* 2016;7:1–8.
 1571 <https://doi.org/10.1038/ncomms10271>.
- 1572 [132] Amara MS, Paineau E, Bacia-Verloop M, Krapf MEM, Davidson P, Belloni L, et
 1573 al. Single-step formation of micron long (OH)₃Al₂O₃Ge(OH) imogolite-like
 1574 nanotubes. *Chem Commun* 2013;49:11284–6.
 1575 <https://doi.org/10.1039/c3cc46839a>.
- 1576 [133] Maillet P, Levard C, Spalla O, Masion A, Rose J, Thill A. Growth kinetic of
 1577 single and double-walled aluminogermanate imogolite-like nanotubes: An
 1578 experimental and modeling approach. *Phys Chem Chem Phys* 2011;13:2682–
 1579 9. <https://doi.org/10.1039/c0cp01851a>.
- 1580 [134] Bottero I, Bonelli B, Ashbrook SE, Wright PA, Zhou W, Tagliabue M, et al.
 1581 Synthesis and characterization of hybrid organic/inorganic nanotubes of the
 1582 imogolite type and their behaviour towards methane adsorption. *Phys Chem*
 1583 *Chem Phys* 2011;13:744–50. <https://doi.org/10.1039/c0cp00438c>.
- 1584 [135] Liao YY, Picot P, Brubach JB, Roy P, Thill A, Le Caër S. Water Adsorption in
 1585 Single- And Double-Walled Inorganic Nanotubes. *J Phys Chem C*
 1586 2019;123:19768–77. <https://doi.org/10.1021/acs.jpcc.9b05621>.
- 1587 [136] Amara MS, Paineau E, Rouzière S, Guiose B, Krapf MEM, Taché O, et al.
 1588 Hybrid, tunable-diameter, metal oxide nanotubes for trapping of organic
 1589 molecules. *Chem Mater* 2015;27:1488–94. <https://doi.org/10.1021/cm503428q>.
- 1590 [137] Liao Y, Picot P, Brubach JB, Roy P, Le Caër S, Thill A. Self-supporting thin
 1591 films of imogolite and imogolite-like nanotubes for infrared spectroscopy. *Appl*
 1592 *Clay Sci* 2018;164:58–67. <https://doi.org/10.1016/j.clay.2017.06.005>.
- 1593 [138] Kang DY, Brunelli NA, Yucelen GI, Venkatasubramanian A, Zang J, Leisen J,
 1594 et al. Direct synthesis of single-walled aminoaluminosilicate nanotubes with
 1595 enhanced molecular adsorption selectivity. *Nat Commun* 2014;5.
 1596 <https://doi.org/10.1038/ncomms4342>.
- 1597 [139] Wang J, Wang Z, Huang B, Ma Y, Liu Y, Qin X, et al. Oxygen vacancy induced
 1598 band-gap narrowing and enhanced visible light photocatalytic activity of ZnO.
 1599 *ACS Appl Mater Interfaces* 2012;4:4024–30.
 1600 <https://doi.org/10.1021/am300835p>.
- 1601 [140] El-Shamy A gamal. New carbon quantum dots nano-particles decorated zinc

- peroxide (Cdots/ZnO₂) nano-composite with superior photocatalytic efficiency for removal of different dyes under UV-A light. *Synth Met* 2020;267:116472. <https://doi.org/10.1016/j.synthmet.2020.116472>.
- [141] Hsu CC, Wu NL. Synthesis and photocatalytic activity of ZnO/ZnO₂ composite. *J Photochem Photobiol A Chem* 2005;172:269–74. <https://doi.org/10.1016/j.jphotochem.2004.12.014>.
- [142] Shafia E, Esposito S, Manzoli M, Chiesa M, Tiberto P, Barrera G, et al. Al/Fe isomorphic substitution versus Fe₂O₃ clusters formation in Fe-doped aluminosilicate nanotubes (imogolite). *J Nanoparticle Res* 2015;17. <https://doi.org/10.1007/s11051-015-3130-2>.
- [143] Shafia E, Esposito S, Armandi M, Manzoli M, Garrone E, Bonelli B. Isomorphic substitution of aluminium by iron into single-walled aluminosilicate nanotubes: A physico-chemical insight into the structural and adsorption properties of Fe-doped imogolite. *Microporous Mesoporous Mater* 2016;224:229–38. <https://doi.org/10.1016/j.micromeso.2015.11.044>.
- [144] Ookawaa M, Inouea Y, Watanabea M, Suzukib M, Yamaguchia T. Synthesis and Characterization of Fe Containing Imogolite. vol. 12. 2006. https://doi.org/https://doi.org/10.11362/jcssjclayscience1960.12.Supplement2_280.
- [145] Guimarães L, Pinto YN, Lourenço MP, Duarte HA. Imogolite-like nanotubes: Structure, stability, electronic and mechanical properties of the phosphorous and arsenic derivatives. *Phys Chem Chem Phys* 2013;15:4303–9. <https://doi.org/10.1039/c3cp44250k>.
- [146] Alvarez-Ramírez F. Theoretical study of (OH)₃N₂O₃MOH, M = C, Si, Ge, Sn and N = Al, Ga, In, with imogolite-like structure. *J Comput Theor Nanosci* 2009;6:1120–4. <https://doi.org/10.1166/jctn.2009.1152>.
- [147] Poli E, Elliott JD, Chulkov SK, Watkins MB, Teobaldi G. The role of cation-vacancies for the electronic and optical properties of aluminosilicate imogolite nanotubes: A non-local, linear-response TDDFT study. *Front Chem* 2019;7:1–17. <https://doi.org/10.3389/fchem.2019.00210>.
- [148] Popov IS, Enyashin AN. Imogolite: Curvature-Induced Hospitality for Trivalent Dopants. *Phys Status Solidi Basic Res* 2021;258:1–9. <https://doi.org/10.1002/pssb.202100188>.
- [149] Li J, Cai L, Shang J, Yu Y, Zhang L. Giant Enhancement of Internal Electric Field Boosting Bulk Charge Separation for Photocatalysis. *Adv Mater* 2016;28:4059–64. <https://doi.org/10.1002/adma.201600301>.
- [150] Wu Y, Gao Z, Li H, Sun X, Li D, Zhou G, et al. Promoting carrier separation efficiently by macroscopic polarization charges and interfacial modulation for photocatalysis. *Chem Eng J* 2021;410. <https://doi.org/10.1016/j.cej.2020.128393>.
- [151] Gao Y, Nie W, Zhu Q, Wang X, Wang S, Fan F, et al. The Polarization Effect in Surface-Plasmon-Induced Photocatalysis on Au/TiO₂ Nanoparticles. *Angew Chemie - Int Ed* 2020;59:18218–23. <https://doi.org/10.1002/anie.202007706>.
- [152] Dong XD, Yao GY, Liu QL, Zhao QM, Zhao ZY. Spontaneous Polarization Effect and Photocatalytic Activity of Layered Compound of BiOIO₃. *Inorg Chem* 2019;58:15344–53. <https://doi.org/10.1021/acs.inorgchem.9b02328>.
- [153] Gustafsson JP. The surface chemistry of imogolite. *Clays Clay Miner* n.d.;49:73–80. <https://doi.org/https://doi.org/10.1346/CCMN.2001.0490106>.
- [154] Elliott JD, Poli E, Scivetti I, Ratcliff LE, Andrinopoulos L, Dziedzic J, et al. Chemically Selective Alternatives to Photoferroelectrics for Polarization-Enhanced Photocatalysis: The Untapped Potential of Hybrid Inorganic

- 1653 Nanotubes. *Adv Sci* 2017;4. <https://doi.org/10.1002/advs.201600153>.
- 1654 [155] Bonelli B, Armandi M, Garrone E. Surface properties of alumino-silicate single-
1655 walled nanotubes of the imogolite type. *Phys Chem Chem Phys*
1656 2013;15:13381–90. <https://doi.org/10.1039/c3cp51508g>.
- 1657 [156] Zanzottera C, Vicente A, Celasco E, Fernandez C, Garrone E, Bonelli B.
1658 Physico-chemical properties of imogolite nanotubes functionalized on both
1659 external and internal surfaces. *J Phys Chem C* 2012;116:7499–506.
1660 <https://doi.org/10.1021/jp301177q>.
- 1661 [157] Patra S, Testard F, Gobeaux F, Sicard L, Shaming D, Caër S Le, et al. UV-
1662 Visible photo-reactivity of permanently polarized inorganic nanotubes coupled
1663 to gold nanoparticles. *Nanoscale* 2023;15:4101–13.
1664 <https://doi.org/10.1039/d2nr05796d>.
- 1665 [158] Kanarek MS. Mesothelioma from Chrysotile Asbestos: Update. *Ann Epidemiol*
1666 2011;21:688–97. <https://doi.org/10.1016/j.annepidem.2011.05.010>.
- 1667 [159] Bernstein D, Dunnigan J, Hesterberg T, Brown R, Velasco JAL, Barrera R, et
1668 al. Health risk of chrysotile revisited. *Crit Rev Toxicol* 2013;43:154–83.
1669 <https://doi.org/10.3109/10408444.2012.756454>.
- 1670 [160] Bernstein DM, Hoskins JA. The health effects of chrysotile: Current
1671 perspective based upon recent data. *Regul Toxicol Pharmacol* 2006;45:252–
1672 64. <https://doi.org/10.1016/j.yrtph.2006.04.008>.
- 1673 [161] Mohanty SK, Gonneau C, Salamatipour A, Pietrofesa RA, Casper B,
1674 Christofidou-Solomidou M, et al. Siderophore-mediated iron removal from
1675 chrysotile: Implications for asbestos toxicity reduction and bioremediation. *J*
1676 *Hazard Mater* 2018;341:290–6. <https://doi.org/10.1016/j.jhazmat.2017.07.033>.
- 1677 [162] Poland CA, Duffin R. The toxicology of chrysotile-containing brake debris:
1678 implications for mesothelioma. *Crit Rev Toxicol* 2019;49:11–35.
1679 <https://doi.org/10.1080/10408444.2019.1568385>.
- 1680 [163] Keija Yada. Study of Microstructure of Chrysotile Asbestos by High Resolution
1681 Electron Microscopy. vol. 12. 1957.
1682 <https://doi.org/https://doi.org/10.1107/S0567739471001402>.
- 1683 [164] Falini G, Foresti E, Gazzano M, Gualtieri AE, Leoni M, Lesci IG, et al. Tubular-
1684 shaped stoichiometric chrysotile nanocrystals. *Chem - A Eur J* 2004;10:3043–
1685 9. <https://doi.org/10.1002/chem.200305685>.
- 1686 [165] Pollastri S, Perchiazzi N, Lezzerini M, Plaisier JR, Cavallo A, Dalconi MC, et
1687 al. The crystal structure of mineral fibres. 1. Chrysotile. *Period Di Mineral*
1688 2016;85:249–59. <https://doi.org/10.2451/2016PM655>.
- 1689 [166] Lesci IG, Balducci G, Pierini F, Soavi F, Roveri N. Surface features and
1690 thermal stability of mesoporous Fe doped geinspired synthetic chrysotile
1691 nanotubes. *Microporous Mesoporous Mater* 2014;197:8–16.
1692 <https://doi.org/10.1016/j.micromeso.2014.06.002>.
- 1693 [167] David SR, Geoffroy VA. A review of asbestos bioweathering by siderophore-
1694 producing pseudomonas: A potential strategy of bioremediation.
1695 *Microorganisms* 2020;8:1–16. <https://doi.org/10.3390/microorganisms8121870>.
- 1696 [168] Foresti E, Gazzano M, Gualtieri AF, Lesci IG, Lunelli B, Pecchini G, et al.
1697 Determination of low levels of free fibres of chrysotile in contaminated soils by
1698 X-ray diffraction and FTIR spectroscopy. *Anal Bioanal Chem* 2003;376:653–8.
1699 <https://doi.org/10.1007/s00216-003-1965-3>.
- 1700 [169] Sprynskyy M, NiedojadŁo J, Buszewski B. Structural features of natural and
1701 acids modified chrysotile nanotubes. *J Phys Chem Solids* 2011;72:1015–26.
1702 <https://doi.org/10.1016/j.jpcs.2011.05.013>.
- 1703 [170] Schwanke AJ, Lopes CW, Pergher SBC. Synthesis of Mesoporous Material

- 1704 from Chrysotile-Derived Silica. *Mater Sci Appl* 2013;04:68–72.
1705 <https://doi.org/10.4236/msa.2013.48a009>.
- 1706 [171] Lourenço MP, De Oliveira C, Oliveira AF, Guimarães L, Duarte HA. Structural,
1707 electronic, and mechanical properties of single-walled chrysotile nanotube
1708 models. *J Phys Chem C* 2012;116:9405–11.
1709 <https://doi.org/10.1021/jp301048p>.
- 1710 [172] Voitylov V V., Voitylov A V., Korytkova EN, Romanov VP, Ul'yanov S V.,
1711 Gusarov V V. Structure of aqueous dispersions of Mg₃Si₂O₅(OH)₄ nanotubes.
1712 *Russ J Appl Chem* 2008;81:207–11.
1713 <https://doi.org/10.1134/s1070427208020092>.
- 1714 [173] López-Salinas E, Toledo-Antonio JA, Manríquez ME, Sánchez-Cantú M, Cruz
1715 Ramos I, Hernández-Cortez JG. Synthesis and catalytic activity of chrysotile-
1716 type magnesium silicate nanotubes using various silicate sources.
1717 *Microporous Mesoporous Mater* 2019;274:176–82.
1718 <https://doi.org/10.1016/j.micromeso.2018.07.041>.
- 1719 [174] Zhang H, Duan T, Zhu W, Yao WT. Natural Chrysotile-Based Nanowires
1720 Decorated with Monodispersed Ag Nanoparticles as a Highly Active and
1721 Reusable Hydrogenation Catalyst. *J Phys Chem C* 2015;119:21465–72.
1722 <https://doi.org/10.1021/acs.jpcc.5b05450>.
- 1723 [175] Ozeki S, Uchiyama H, Katada M. Hydrolysis of Iron Ion in Chrysotile
1724 Nanotubules: A Template Effect on Crystal Growth. *Langmuir* 1994;10:923–8.
1725 <https://doi.org/10.1021/la00015a051>.
- 1726 [176] Peng Q, Dai Y, Liu K, Tang X, Zhou M, Zhang Y, et al. Outstanding catalytic
1727 performance of metal-free peroxymonosulfate activator: Important role of
1728 chrysotile. *Sep Purif Technol* 2022;287:120526.
1729 <https://doi.org/10.1016/j.seppur.2022.120526>.
- 1730 [177] Nakagaki S, Castro KADF, Machado GS, Halma M, Drechsel SM, Wypych F.
1731 Catalytic activity in oxidation reactions of anionic iron(III) porphyrins
1732 immobilized on raw and grafted chrysotile. *J Braz Chem Soc* 2006;17:1672–8.
1733 <https://doi.org/10.1590/S0103-50532006000800027>.
- 1734 [178] Chen H, Wan K, Zheng F, Zhang Z, Zhang Y, Long D. Mechanism insight into
1735 photocatalytic conversion of lignin for valuable chemicals and fuels production:
1736 A state-of-the-art review. *Renew Sustain Energy Rev* 2021;147:111217.
1737 <https://doi.org/10.1016/j.rser.2021.111217>.
- 1738 [179] Lang X, Chen X, Zhao J. Heterogeneous visible light photocatalysis for
1739 selective organic transformations. *Chem Soc Rev* 2014;43:473–86.
1740 <https://doi.org/10.1039/c3cs60188a>.
- 1741 [180] Pouthika K, Madhumitha G. A Mini Review on Recent Advancements in Metal
1742 Oxide Integrated Nano-Tubular Inorganic Clay Mineral Photocatalyst for
1743 Organic Pollutant Degradation. *Comments Inorg Chem* 2024;00:1–33.
1744 <https://doi.org/10.1080/02603594.2024.2312395>.
- 1745 [181] Li Y, Yuan X, Jiang L, Dai H, Zhao Y, Guan X, et al. Manipulation of the
1746 halloysite clay nanotube lumen for environmental remediation: a review.
1747 *Environ Sci Nano* 2022;9:841–66. <https://doi.org/10.1039/d1en01032h>.
- 1748 [182] Liu J, Zhang G. Recent advances in synthesis and applications of clay-based
1749 photocatalysts: A review. *Phys Chem Chem Phys* 2014;16:8178–92.
1750 <https://doi.org/10.1039/c3cp54146k>.
- 1751 [183] Jing G, Sun Z, Ye P, Wei S, Liang Y. Clays for heterogeneous photocatalytic
1752 decolorization of wastewaters contaminated with synthetic dyes: A review.
1753 *Water Pract Technol* 2017;12:432–43. <https://doi.org/10.2166/wpt.2017.046>.
- 1754 [184] Zou Y, Hu Y, Shen Z, Yao L, Tang D, Zhang S, et al. Application of

- 1755 aluminosilicate clay mineral-based composites in photocatalysis. *J Environ Sci*
 1756 (China) 2022;115:190–214. <https://doi.org/10.1016/j.jes.2021.07.015>.
- 1757 [185] Papoulis D. Halloysite based nanocomposites and photocatalysis: A Review.
 1758 *Appl Clay Sci* 2019;168:164–74. <https://doi.org/10.1016/j.clay.2018.11.009>.
- 1759 [186] Imgharn A, Anchoum L, Hsini A, Naciri Y, Laabd M, Mobarak M, et al.
 1760 Effectiveness of a novel polyaniline@Fe-ZSM-5 hybrid composite for Orange
 1761 G dye removal from aqueous media: Experimental study and advanced
 1762 statistical physics insights. *Chemosphere* 2022;295.
 1763 <https://doi.org/10.1016/j.chemosphere.2022.133786>.
- 1764 [187] Bhatia D, Sharma NR, Singh J, Kanwar RS. Biological methods for textile dye
 1765 removal from wastewater: A review. *Crit Rev Environ Sci Technol*
 1766 2017;47:1836–76. <https://doi.org/10.1080/10643389.2017.1393263>.
- 1767 [188] Katheresan V, Kansedo J, Lau SY. Efficiency of various recent wastewater dye
 1768 removal methods: A review. *J Environ Chem Eng* 2018;6:4676–97.
 1769 <https://doi.org/10.1016/j.jece.2018.06.060>.
- 1770 [189] Hsini A, Naciri Y, Bouziani A, Aarab N, Essekre A, Imgharn A, et al. Polyaniline
 1771 coated tungsten trioxide as an effective adsorbent for the removal of orange G
 1772 dye from aqueous media. *RSC Adv* 2021;11:31272–83.
 1773 <https://doi.org/10.1039/d1ra04135e>.
- 1774 [190] Ali H, Ahmed S, Hsini A, Kizito S, Naciri Y, Djellabi R, et al.
 1775 Adsorption/desorption characteristics of novel Fe₃O₄ impregnated N-doped
 1776 biochar (Fe₃O₄@N/BC) for arsenic (III and V) removal from aqueous solution:
 1777 Insight into mechanistic understanding and reusability potential. *Arab J Chem*
 1778 2022;104209. <https://doi.org/10.1016/j.arabjc.2022.104209>.
- 1779 [191] Brini L, Hsini A, Naciri Y, Bouziani A, Ajmal Z, H'Maida K, et al. Synthesis and
 1780 characterization of arginine-doped heliotrope leaves with high clean-up
 1781 capacity for crystal violet dye from aqueous media. *Water Sci Technol*
 1782 2021;84:2265–77. <https://doi.org/10.2166/wst.2021.446>.
- 1783 [192] Sudarjanto G, Keller-Lehmann B, Keller J. Optimization of integrated chemical-
 1784 biological degradation of a reactive azo dye using response surface
 1785 methodology. *J Hazard Mater* 2006;138:160–8.
 1786 <https://doi.org/10.1016/j.jhazmat.2006.05.054>.
- 1787 [193] Naciri Y, Ahdour A, Benhsina E, Hamza MA, Bouziani A, Hsini A, et al.
 1788 Ba₃(PO₄)₂ Photocatalyst for Efficient Photocatalytic Application. *Glob*
 1789 *Challenges* 2023;3:1–11. <https://doi.org/10.1002/gch2.202300257>.
- 1790 [194] Wu D, Li J, Guan J, Liu C, Zhao X, Zhu Z, et al. Improved photoelectric
 1791 performance via fabricated heterojunction g-C₃N₄/TiO₂/HNTs loaded
 1792 photocatalysts for photodegradation of ciprofloxacin. *J Ind Eng Chem*
 1793 2018;64:206–18. <https://doi.org/10.1016/j.jiec.2018.03.017>.
- 1794 [195] Li X, Zhu W, Yan X, Lu X, Yao C, Ni C. Hierarchical
 1795 La_{0.7}Ce_{0.3}FeO₃/halloysite nanocomposite for photocatalytic degradation of
 1796 antibiotics. *Appl Phys A Mater Sci Process* 2016;122:1–5.
 1797 <https://doi.org/10.1007/s00339-016-0240-3>.
- 1798 [196] Jatav S, Xiang H, Herber M, Paineau E, Hill EH. In₂S₃ Growth Templated by
 1799 Aluminogermanate Double-Walled Imogolite Nanotubes Toward Efficient
 1800 Visible Light Photocatalysts. *Sol RRL* 2023;7:3–8.
 1801 <https://doi.org/10.1002/solr.202200947>.
- 1802 [197] Zhang Y, Yang H. Co₃O₄ nanoparticles on the surface of halloysite
 1803 nanotubes. *Phys Chem Miner* 2012;39:789–95.
 1804 <https://doi.org/10.1007/s00269-012-0533-9>.
- 1805 [198] Peng H, Wu D, Wan H, Jia LL, Chen G, Li J, et al. Facile synthesis and

- 1806 characterization of halloysite@W18O49 nanocomposite with enhanced
 1807 photocatalytic properties. *Appl Clay Sci* 2019;183.
 1808 <https://doi.org/10.1016/j.clay.2019.105319>.
- 1809 [199] Peng H, Zhang D, Liu X, Tang W, Wan H, Xiong H, et al. Facile synthesis and
 1810 characterization of core-shell structured Ag₃PO₄@Hal nanocomposites for
 1811 enhanced photocatalytic properties. *Appl Clay Sci* 2017;141:132–7.
 1812 <https://doi.org/10.1016/j.clay.2017.02.023>.
- 1813 [200] Christoforidis KC, Melchionna M, Montini T, Papoulis D, Stathatos E,
 1814 Zafeiratos S, et al. Solar and visible light photocatalytic enhancement of
 1815 halloysite nanotubes/g-C₃N₄ heteroarchitectures. *RSC Adv* 2016;6:86617–26.
 1816 <https://doi.org/10.1039/c6ra15581b>.
- 1817 [201] Krasilin AA, Bodalyov IS, Malkov AA, Khrapova EK, Maslennikova TP, Malygin
 1818 AA. On an adsorption/photocatalytic performance of nanotubular
 1819 Mg₃Si₂O₅(OH)₄/TiO₂ composite. *Nanosyst Physics, Chem Math* 2018:410–6.
 1820 <https://doi.org/10.17586/2220-8054-2018-9-3-410-416>.
- 1821 [202] Bahadori E, Vaiano V, Esposito S, Armandi M, Sannino D, Bonelli B. Photo-
 1822 activated degradation of tartrazine by H₂O₂ as catalyzed by both bare and Fe-
 1823 doped methyl-imogolite nanotubes. *Catal Today* 2018;304:199–207.
 1824 <https://doi.org/10.1016/j.cattod.2017.08.003>.
- 1825 [203] Szczepanik B, Rogala P, Słomkiewicz PM, Banaś D, Kubala-Kukuś A,
 1826 Stabrawa I. Synthesis, characterization and photocatalytic activity of TiO₂-
 1827 halloysite and Fe₂O₃-halloysite nanocomposites for photodegradation of
 1828 chloroanilines in water. *Appl Clay Sci* 2017;149:118–26.
 1829 <https://doi.org/10.1016/j.clay.2017.08.016>.
- 1830 [204] Nyankson E, Kumar R V. Removal of water-soluble dyes and pharmaceutical
 1831 wastes by combining the photocatalytic properties of Ag₃PO₄ with the
 1832 adsorption properties of halloysite nanotubes. *Mater Today Adv* 2019;4.
 1833 <https://doi.org/10.1016/j.mtadv.2019.100025>.
- 1834 [205] Guan J, Li J, Ye Z, Wu D, Liu C, Wang H, et al. La₂O₃ media enhanced
 1835 electrons transfer for improved CeVO₄ @halloysite nanotubes photocatalytic
 1836 activity for removing tetracycline. *J Taiwan Inst Chem Eng* 2019;96:281–98.
 1837 <https://doi.org/10.1016/j.jtice.2018.10.030>.
- 1838 [206] Cheng ZL, Sun W. Preparation and Solar Light Photocatalytic Activity of N-
 1839 Doped TiO₂-Loaded Halloysite Nanotubes Nanocomposites. *J Mater Eng*
 1840 *Perform* 2015;24:4090–5. <https://doi.org/10.1007/s11665-015-1699-3>.
- 1841 [207] Nyankson E, Agyei-Tuffour B, Annan E, Yaya A, Mensah B, Onwona-
 1842 Agyeman B, et al. Ag₂CO₃-halloysite nanotubes composite with enhanced
 1843 removal efficiency for water soluble dyes. *Heliyon* 2019;5.
 1844 <https://doi.org/10.1016/j.heliyon.2019.e01969>.
- 1845 [208] Xing W, Ni L, Huo P, Lu Z, Liu X, Luo Y, et al. Preparation high photocatalytic
 1846 activity of CdS/halloysite nanotubes (HNTs) nanocomposites with
 1847 hydrothermal method. *Appl Surf Sci* 2012;259:698–704.
 1848 <https://doi.org/10.1016/j.apsusc.2012.07.102>.
- 1849 [209] Xu J, Zhang B, Jia L, Bi N, Zhao T. Metal-enhanced fluorescence detection
 1850 and degradation of tetracycline by silver nanoparticle-encapsulated halloysite
 1851 nano-lumen. *J Hazard Mater* 2020;386.
 1852 <https://doi.org/10.1016/j.jhazmat.2019.121630>.
- 1853 [210] Wu H, Jian W, Zhang L, Lin J, Li J. Boosting carrier separation in
 1854 Ag/AgBr/halloysite-nanotubes composites for enhanced photocatalytic
 1855 performance. *Mater Sci Semicond Process* 2021;121.
 1856 <https://doi.org/10.1016/j.mssp.2020.105373>.

- 1857 [211] Zou M, Du M, Zhu H, Xu C, Fu Y. Green synthesis of halloysite nanotubes
1858 supported Ag nanoparticles for photocatalytic decomposition of methylene
1859 blue. *J Phys D Appl Phys* 2012;45. [https://doi.org/10.1088/0022-](https://doi.org/10.1088/0022-3727/45/32/325302)
1860 [3727/45/32/325302](https://doi.org/10.1088/0022-3727/45/32/325302).
- 1861 [212] Xing W, Ni L, Liu X, Luo Y, Lu Z, Yan Y, et al. Effect of metal ion (Zn²⁺, Bi³⁺,
1862 Cr³⁺, and Ni²⁺)-doped CdS/halloysite nanotubes (HNTs) photocatalyst for the
1863 degradation of tetracycline under visible light. *Desalin Water Treat*
1864 2015;53:794–805. <https://doi.org/10.1080/19443994.2013.844082>.
- 1865 [213] Wang H, Wu D, Li X, Huo P. Ce doping TiO₂/halloysite nanotubes
1866 photocatalyst for enhanced electrons transfer and photocatalytic degradation
1867 of Tetracycline. *J Mater Sci Mater Electron* 2019;30:19126–36.
1868 <https://doi.org/10.1007/s10854-019-02268-y>.
- 1869 [214] Jiang L, Huang Y, Liu T. Enhanced visible-light photocatalytic performance of
1870 electrospun carbon-doped TiO₂/halloysite nanotube hybrid nanofibers. *J*
1871 *Colloid Interface Sci* 2015;439:62–8. <https://doi.org/10.1016/j.jcis.2014.10.026>.
- 1872 [215] Li C, Zhou T, Zhu T, Li X. Enhanced visible light photocatalytic activity of
1873 polyaniline-crystalline TiO₂-halloysite composite nanotubes by tuning the acid
1874 dopant in the preparation. *RSC Adv* 2015;5:98482–91.
1875 <https://doi.org/10.1039/c5ra20024e>.
- 1876 [216] Zheng P, Du Y, Chang PR, Ma X. Amylose-halloysite-TiO₂ composites:
1877 Preparation, characterization and photodegradation. *Appl Surf Sci*
1878 2015;329:256–61. <https://doi.org/10.1016/j.apsusc.2014.12.158>.
- 1879 [217] Gesesse GD, Le Neel T, Cui Z, Bachelier G, Remita H, Colbeau-Justin C, et
1880 al. Plasmonic core-shell nanostructure as an optical photoactive nanolens for
1881 enhanced light harvesting and hydrogen production. *Nanoscale*
1882 2018;10:20140–6. <https://doi.org/10.1039/c8nr07475e>.
- 1883 [218] Hojamberdiev M, Khan MM, Kadirova Z, Kawashima K, Yubuta K, Teshima K,
1884 et al. Synergistic effect of g-C₃N₄, Ni(OH)₂ and halloysite in nanocomposite
1885 photocatalyst on efficient photocatalytic hydrogen generation. *Renew Energy*
1886 2019;138:434–44. <https://doi.org/10.1016/j.renene.2019.01.103>.
- 1887 [219] Lu J, Lin H, Hong R, Zhang D. Photocatalytic H₂ evolution properties of
1888 K_{0.5}Na_{0.5}NbO₃ (KNN) with halloysite nanotubes. *Opt Mater (Amst)* 2022;129.
1889 <https://doi.org/10.1016/j.optmat.2022.112516>.
- 1890 [220] Jimenéz-Calvo P, Naciri Y, Sobolewska A, Isaacs M, Zhang Y, Leforestier A,
1891 et al. Ti-Modified Imogolite Nanotubes as Promising Photocatalyst 1D
1892 Nanostructures for H₂ Production. *Small Methods* 2023;2301369:1–10.
1893 <https://doi.org/10.1002/smt.202301369>.
- 1894 [221] Lin S, Zhang Y, You Y, Zeng C, Xiao X, Ma T, et al. Bifunctional Hydrogen
1895 Production and Storage on 0D–1D Heterojunction of
1896 Cd_{0.5}Zn_{0.5}S@Halloysites. *Adv Funct Mater* 2019;29.
1897 <https://doi.org/10.1002/adfm.201903825>.
- 1898 [222] Lasek J, Yu YH, Wu JCS. Removal of NO_x by photocatalytic processes. *J*
1899 *Photochem Photobiol C Photochem Rev* 2013;14:29–52.
1900 <https://doi.org/10.1016/j.jphotochemrev.2012.08.002>.
- 1901 [223] Ângelo J, Andrade L, Madeira LM, Mendes A. An overview of photocatalysis
1902 phenomena applied to NO_x abatement. *J Environ Manage* 2013;129:522–39.
1903 <https://doi.org/10.1016/j.jenvman.2013.08.006>.
- 1904 [224] Papoulis D, Komarneni S, Nikolopoulou A, Tsolis-Katagas P, Panagiotaras D,
1905 Kacandes HG, et al. Palygorskite- and Halloysite-TiO₂ nanocomposites:
1906 Synthesis and photocatalytic activity. *Appl Clay Sci* 2010;50:118–24.
1907 <https://doi.org/10.1016/j.clay.2010.07.013>.

- 1908 [225] Papoulis D, Komarneni S, Panagiotaras D, Stathatos E, Christoforidis KC,
1909 Fernández-García M, et al. Three-phase nanocomposites of two nanoclays
1910 and TiO₂: Synthesis, characterization and photocatalytic activities. *Appl Catal*
1911 *B Environ* 2014;147:526–33. <https://doi.org/10.1016/j.apcatb.2013.09.025>.
- 1912 [226] Laxma Reddy PV, Kavitha B, Kumar Reddy PA, Kim KH. TiO₂-based
1913 photocatalytic disinfection of microbes in aqueous media: A review. *Environ*
1914 *Res* 2017;154:296–303. <https://doi.org/10.1016/j.envres.2017.01.018>.
- 1915 [227] Cai Y, Sun T, Li G, An T. Traditional and Emerging Water Disinfection
1916 Technologies Challenging the Control of Antibiotic-Resistant Bacteria and
1917 Antibiotic Resistance Genes. *ACS ES&T Eng* 2021;1:1046–64.
1918 <https://doi.org/10.1021/acsestengg.1c00110>.
- 1919 [228] Pichel N, Vivar M, Fuentes M. The problem of drinking water access: A review
1920 of disinfection technologies with an emphasis on solar treatment methods.
1921 *Chemosphere* 2019;218:1014–30.
1922 <https://doi.org/10.1016/j.chemosphere.2018.11.205>.
- 1923 [229] Ipek Yucelen G, Connell RE, Terbush JR, Westenberg DJ, Dogan F. Synthesis
1924 and immobilization of silver nanoparticles on aluminosilicate nanotubes and
1925 their antibacterial properties. *Appl Nanosci* 2016;6:607–14.
1926 <https://doi.org/10.1007/s13204-015-0467-x>.
- 1927 [230] Geraldo DA, Arancibia-Miranda N, Villagra NA, Mora GC, Arratia-Perez R.
1928 Synthesis of CdTe QDs/single-walled aluminosilicate nanotubes hybrid
1929 compound and their antimicrobial activity on bacteria. *J Nanoparticle Res*
1930 2012;14. <https://doi.org/10.1007/s11051-012-1286-6>.
- 1931